$FOXP3^+$ $CD4^+$ T cell population in our humanized mouse model is Tregs. Moreover, the expression level of CCR5, an HIV-1 coreceptor, was higher on Tregs than on Tms and Tns in both humans and humanized mice (Figure 1C and 1D). Furthermore, in line with previous studies reporting that Tregs actively proliferate *in vivo* [9–11], the percentage of the cells positive for MKI67 antigen identified by monoclonal antibody Ki-67 (MKI67; also known as Ki67) in Tregs of humans and humanized mice was significantly higher than those in Tms and Tns (Figure 1C and 1D). These results indicate that Tregs in humans and humanized mice are more actively cycling than Tns and Tms. Altogether, these results suggested that the profile and characteristics of $CD4^+$ T cell subsets in humanized mice mirror those in healthy humans.

To investigate the dynamics of each $CD4^+$ T cell subset after HIV-1 infection, 40 humanized mice were infected with a primary R5 HIV-1 isolate, strain JR-CSF [30]. As observed in HIV-1-infected individuals [15–17] and SIV-infected monkeys [18–20], we found that Tregs were preferentially and significantly decreased in the peripheral blood (PB) (Figure 2A and 2B) and the spleen (Figure 2C and 2D) of HIV-1-infected humanized mice until 21 days postinfection (dpi). However, because we have previously observed that surface CD4 molecules on HIV-1-infected cells in humanized mice are downregulated [21,23], we evaluated whether this was the case in Tregs. Results showed that Tregs were positive for surface CD4 (i.e., $CD4^-$ $FOXP3^+$ cells were absent) (Figure S1), indicating that the disappearance of Tregs during the acute phase of infection was not due to surface CD4 down-regulation, but rather to depletion by HIV-1 infection. Since CCR5 is highly expressed on Tregs (Figure 1C and 1D), we further assessed the level of $CCR5^+$ $CD4^+$ T cells in R5 HIV-1-infected humanized mice. As shown in Figure 2E, we observed zthat the percentage of $CCR5^+$ cells in the splenic $CD4^+$ T cells of R5 HIV-1-infected mice was significantly lower than that of mock-infected mice (Figure 2E). These findings suggest that R5 HIV-1 infection induces severe depletion of $CCR5^+$ $CD4^+$ T cells including Tregs during acute infection.

It is well known that Tregs have the potential to suppress immune activation *in vivo*, and that the depletion of Tregs induces aberrant immune activation [7]. To address this possibility in HIV-1-infected humanized mice, we assessed the immune activation status at 21 dpi by staining with CD38, an activation marker [31,32]. As shown in Figure 2F, the expression level of CD38 on memory $CD8^+$ T cells in the spleen of HIV-1-infected mice was significantly higher than that of mock-infected mice.

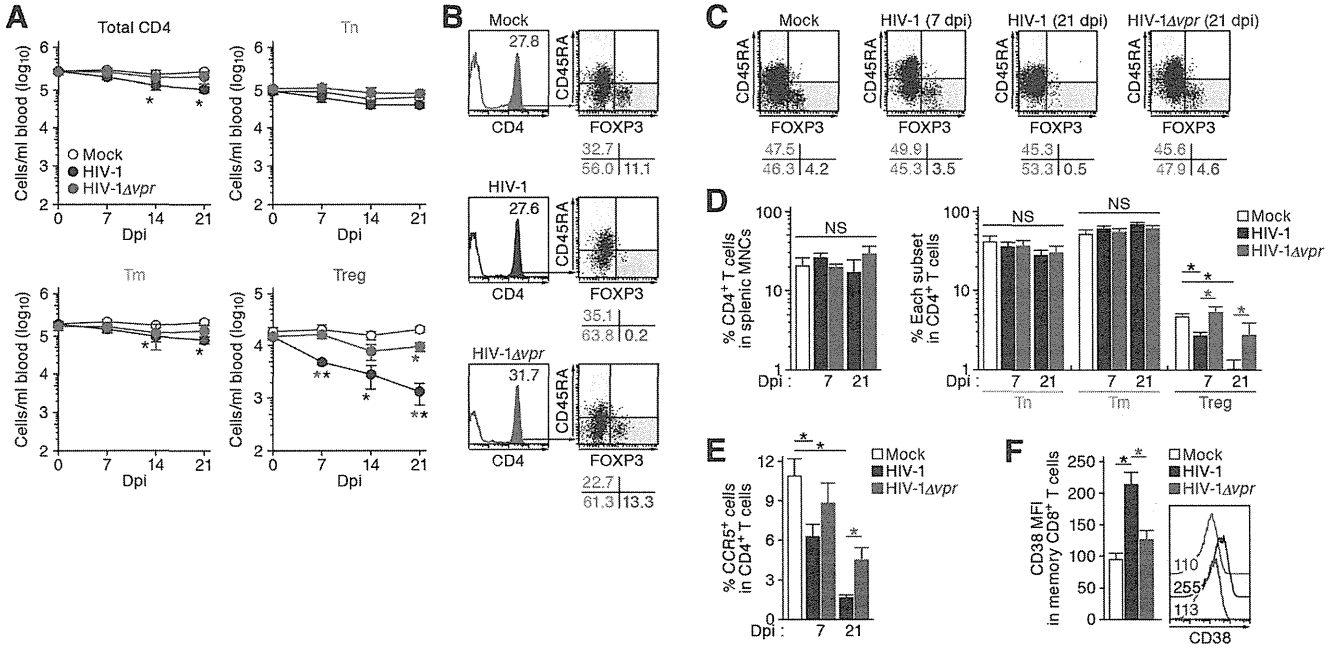

Figure 2. Dynamics of human $CD4^+$ T cell subsets in humanized mice infected with R5 WT and *vpr*-deficient HIV-1. (A and B) Longitudinal analyses of the dynamics of human $CD4^+$ T cell subsets in the PB of infected humanized mice. The numbers of total $CD4^+$ T cells ($CD45^+$ $CD3^+$ $CD4^+$ cells), Tns ($CD45^+$ $CD3^+$ $CD4^+$ $CD45RA^+$ $FOXP3^-$ cells), Tms ($CD45^+$ $CD3^+$ $CD4^+$ $CD45RA^-$ $FOXP3^-$ cells), and Tregs ($CD45^+$ $CD3^+$ $CD4^+$ $CD45RA^-$ $FOXP3^+$ cells) in the PB of R5 WT HIV-1-infected mice (n = 8), R5 *vpr*-deficient HIV-1-infected mice (n = 8), and mock-infected mice (n = 12) were routinely quantified by flow cytometry and hematocytometry. Summarized results (A) and representative dot plots at 21 dpi (B) are shown, respectively. In panel B, the numbers in the histogram indicate the percentage of $CD4^+$ cells in $CD45^+$ cells, and the numbers under the dot plots indicate the percentage of the cells in each quadrant. (C and D) Cytopathic effect of WT and *vpr*-deficient HIV-1 in the spleen of humanized mice. The percentages of total $CD4^+$ T cells, Tns, Tms, and Tregs in the splenic MNCs of WT HIV-1-infected mice (7 dpi, n = 19; 21 dpi, n = 8), *vpr*-deficient HIV-1-infected mice (7 dpi, n = 10; 21 dpi, n = 7), and mock-infected mice (n = 12) were routinely quantified by flow cytometry. Representative dot plots (C) and summarized results (D) are shown, respectively. In panel C, the numbers under the dot plots indicate the percentage of the cells in each quadrant. (E) The level of CCR5-expressing $CD4^+$ T cells in infected humanized mice. The percentage of $CCR5^+$ cells in the splenic $CD4^+$ T cells of WT HIV-1-infected mice (7 dpi, n = 8; 21 dpi, n = 6), *vpr*-deficient HIV-1-infected mice (7 dpi, n = 8; 21 dpi, n = 6), and mock-infected mice (n = 8) was analyzed by flow cytometry. (F) The level of immune activation in infected humanized mice. The MFI of CD38 in memory $CD8^+$ T cells ($CD45^+$ $CD3^+$ $CD8^+$ $CD45RA^-$ cells) in the spleen of WT HIV-1-infected mice (n = 5), *vpr*-deficient HIV-1-infected mice (n = 5), and mock-infected mice (n = 5) at 21 dpi was analyzed by flow cytometry. Representative histograms are shown on the right panel, and the numbers in the histogram indicate the MFI values. Statistical difference was determined by Welch's *t* test, and statistically significant differences ($P<0.05$) are shown as follows: mock versus WT HIV-1, black asterisk; mock versus HIV-1*Δvpr*, blue asterisk; and WT HIV-1 versus HIV-1*Δvpr*, red asterisk. NS, no statistical significance. Data represent mean ± SEM.

doi:10.1371/journal.ppat.1003812.g002

These results suggested that HIV-1 infection decreased Tregs in humanized mice and resulted in immune activation.

Vpr depletes Tregs and enhances HIV-1 propagation in a coreceptor-dependent manner

As described in Introduction section, Vpr is pleiotropic and is known to induce cell cycle arrest at the G_2 phase and apoptosis [1]. Since Tregs are highly proliferative *in vivo* (Figure 1), which is consistent with previous reports [9–11], we hypothesized that Tregs are highly susceptible to Vpr-mediated G_2 arrest. To test this hypothesis, 32 humanized mice were infected with R5 *vpr*-deficient HIV-1 (HIV-1*Δvpr*; strain JR-CSF) [33]. Although the infectivities of R5 WT HIV-1 and R5 HIV-1*Δvpr* were comparable *in vitro* (Figure S2), the level of viral load in the plasma of HIV-1*Δvpr*-infected mice at 4 and 7 dpi was significantly lower than that of WT HIV-1-infected mice (Figure 3A). These results suggested that HIV-1*Δvpr* is less replicative than WT HIV-1 during initial stage of infection in humanized mice. We also investigated the dynamics of $CD4^+$ T cells in HIV-1*Δvpr*-infected mice and found that the acute and severe depletion of Tregs after virus challenge was not observed in the PB (Figure 2A and 2B) and the spleen (Figure 2C and 2D). In addition, the level of $CCR5^+$ $CD4^+$ T cells in the spleen of HIV-1*Δvpr*-infected mice was significantly higher than that of WT HIV-1-infected mice (Figure 2E). Moreover, the immune activation, which was observed in WT HIV-1-infected mice, was not detected in HIV-1*Δvpr*-infected mice (Figure 2F). These findings suggested that Vpr enhances virus dissemination and induces Treg depletion leading to immune activation in humanized mice.

To address the association of Vpr with the rapid HIV-1 expansion *in vivo*, we next assessed the distribution of HIV-1-infected cells during acute infection (i.e., 7 dpi). As shown in Figure 3B, the percentage of the cells positive for p24, an HIV-1 antigen, in splenic $CD3^+$ $CD8^-$ cells of WT HIV-1-infected mice was comparable to that of HIV-1*Δvpr*-infected mice. We then examined the proportion of $p24^+$ cells in each $CD4^+$ T cell subset and found that Tregs were more positive for p24 than Tm and Tn in both WT HIV-1-infected and HIV-1*Δvpr*-infected mice (Figure 3C, left and right panels). In addition, we demonstrated that the percentage of $p24^+$ Tregs in WT HIV-1-infected mice was significantly higher than that in HIV-1*Δvpr*-infected mice (Figure 3C, left and right panels). Moreover, in WT HIV-1 but not in HIV-1*Δvpr*-infected mice, the mean fluorescent intensity (MFI) of p24, which reflects the expression level of viral proteins in infected cells, was significantly higher in Tregs than in Tns and Tms (Figure 3C, middle and right panels). Taken together, these results suggested that Tregs were highly susceptible to HIV-1 infection and produced large amounts of the virus with Vpr responsible for augmenting this production.

These findings raised the possibility that the preferential HIV-1 infection in Tregs was due to their high CCR5 expression (Figure 1C and 1D). To demonstrate this possibility, we assessed the expression level of CXCR4, another coreceptor for HIV-1, in each $CD4^+$ T cell subset. In both humans and humanized mice, we found that CXCR4 was broadly expressed in all $CD4^+$ T cell subsets and was highly expressed on Tns than Tms and Tregs (Figure 4A and 4B). Then, 13 humanized mice were infected with an X4 WT HIV-1 (strain NL4-3) [34], while 11 humanized mice were infected with an X4 HIV-1*Δvpr* (strain NL4-3) [2]. The infectivities of X4 WT HIV-1 and X4 HIV-1*Δvpr* were comparable *in vitro* (Figure S3). In contrast to the observations in R5 HIV-1-infected humanized mice (Figure 3A), the viral load of X4 WT HIV-1 and was comparable to that of X4 *vpr*-deficient HIV-1 (Figure 4C). In addition, the depletion of Tregs during the acute phase of infection, which was found in R5 HIV-1-infected mice (Figure 2A–2D), was not observed in the PB (Figure 4D) and the spleen (Figure 4E and 4F) of X4 WT HIV-1-infected mice. Furthermore, we did not observe the immune activation in X4 HIV-1-infected mice during acute infection (Figure 4G). Taken together, these findings strongly suggest that the preferential HIV-1 infection and the Treg depletion leading to immune activation during acute infection are dependent on the coreceptor usage of HIV-1.

Vpr induces a significant level of G_2 cell cycle arrest in infected Tregs

Extensive *in vitro* studies have reported that Vpr can cause cell cycle arrest at the G_2 phase [1]. To investigate the cell cycle condition of R5 HIV-1-infected cells in humanized mice at 7 dpi, cellular DNA content was quantified by Hoechst staining. Although the percentages of p24-negative cells at the G_2M phase in the spleen of WT HIV-1-infected and HIV-1*Δvpr*-infected cells were similar to those of mock-infected mice, a significant level of p24-positive cells at the G_2M phase in both WT HIV-1-infected and HIV-1*Δvpr*-infected mice were detected (Figure 5A). Moreover, we found that the percentage of $p24^+$

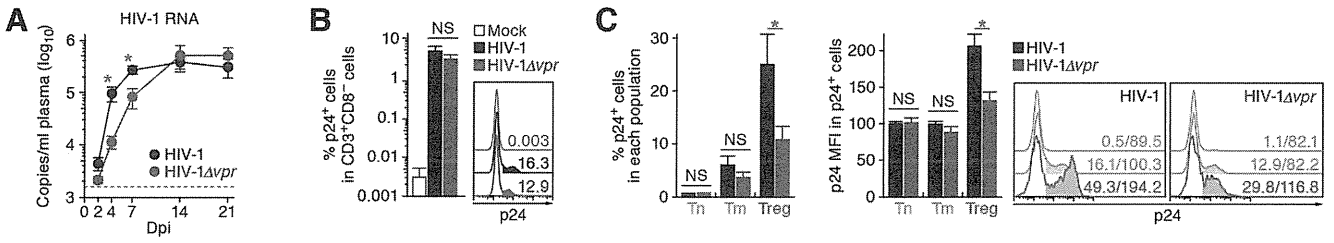

Figure 3. Dynamics of R5 WT and *vpr*-deficient HIV-1 infection in humanized mice. (A) Viral load in infected humanized mice. The amounts of viral RNA in the plasma of R5 WT HIV-1-infected mice (n = 30) and R5 *vpr*-deficient HIV-1-infected mice (n = 23) were routinely quantified. The horizontal broken line indicates the detection limit of the assay (1,600 copies/ml). (B and C) Infected cells in humanized mice. HIV-1-infected cells in the spleen of R5 WT HIV-1-infected mice (n = 19), R5 *vpr*-deficient HIV-1-infected mice (n = 10), and mock-infected mice (n = 10) at 7 dpi were analyzed by flow cytometry using an anti-HIV-1 p24 antibody. The percentages of $p24^+$ cells in $CD3^+$ $CD8^-$ cells (B) and in each $CD4^+$ T cell subset (C, left panel), and the MFI of p24 in $p24^+$ cells of each $CD4^+$ T cell subset (C, middle panel) are shown. Representative histograms are shown on the right panel. In panel B, the numbers in the histogram indicate the positivity. In panel C, the numbers in the histogram indicate the percentage of positive cells (left) and MFI values (right). Statistical difference was determined by Welch's *t* test, and statistically significant differences between WT HIV-1 versus HIV-1*Δvpr* ($P<0.05$) are shown with red asterisks. NS, no statistical significance. Data represent mean ± SEM.
doi:10.1371/journal.ppat.1003812.g003

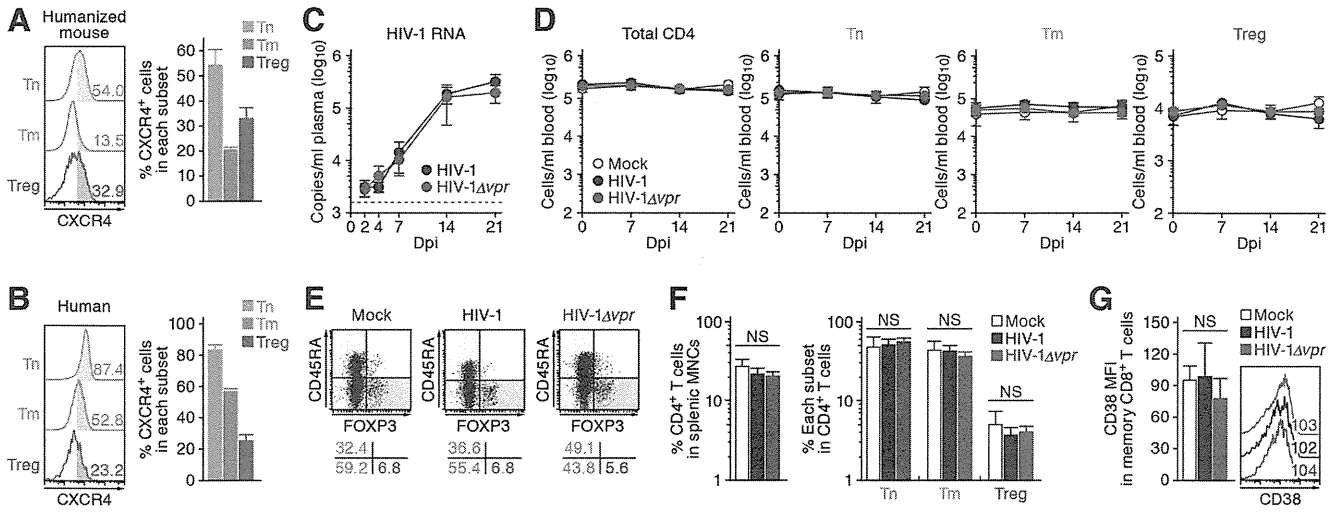

Figure 4. Dynamics of X4 WT and *vpr*-deficient HIV-1 infection in humanized mice. (A and B) CXCR4 expression on $CD4^+$ T cell subsets in human and humanized mouse. Human $CD4^+$ T cells isolated from the spleen of humanized mice (A, n = 8) and the PB of HIV seronegative humans (B, n = 6) were classified into Tn, Tm, and Treg as described in the legend of Figure 1. Representative dot plots and histograms are shown on the left, and the percentages of $CXCR4^+$ cells in each subset are shown on the right. In the left panels, the numbers in each histogram indicate the positivity. (C) Viral load in infected humanized mice. The amounts of viral RNA in the plasma of X4 WT HIV-1-infected mice (n = 13) and X4 *vpr*-deficient HIV-1-infected mice (n = 11) were routinely quantified. The horizontal broken line indicates the detection limit of the assay (1,600 copies/ml). (D) Longitudinal analyses of the dynamics of human $CD4^+$ T cell subsets in the PB of infected humanized mice. The numbers of total $CD4^+$ T cells, Tns, Tms, and Tregs in the PB of WT HIV-1-infected mice (n = 9), *vpr*-deficient HIV-1-infected mice (n = 9), and mock-infected mice (n = 8) were routinely quantified by flow cytometry and hematocytometry. (E and F) Cytopathic effect of WT and *vpr*-deficient HIV-1 in the spleen of humanized mice. The percentages of total $CD4^+$ T cells, Tns, Tms, and Tregs in the splenic MNCs of WT HIV-1-infected mice (n = 8), *vpr*-deficient HIV-1-infected mice (n = 8), and mock-infected mice (n = 8) at 21 dpi were routinely quantified by flow cytometry. Representative dot plots (E) and summarized results (F) are shown, respectively. In panel E, the numbers on the right of the dot plots indicate the percentage of the cells in each quadrant. (G) The level of immune activation in infected humanized mice. The MFI of CD38 in memory $CD8^+$ T cells in the spleen of WT HIV-1-infected mice (n = 5), *vpr*-deficient HIV-1-infected mice (n = 5), and mock-infected mice (n = 5) at 21 dpi was analyzed by flow cytometry. Representative histograms are shown on the right panel, and the numbers in the histogram indicate the MFI values. NS, no statistical significance. Data represent mean ± SEM.
doi:10.1371/journal.ppat.1003812.g004

cells at the G_2M phase in WT HIV-1-infected mice was significantly higher than that in HIV-1*Δvpr*-infected mice (Figure 5A), suggesting that Vpr expressed in infected cells induced G_2 cell cycle arrest *in vivo*.

We next analyzed the level of G_2 arrest in each $CD4^+$ T cell subset. Since $p24^+$ cells were faintly detected in the Tn subset (Figure 3C; 0.33±0.1% for WT HIV-1, 0.35±0.1% for HIV-1*Δvpr*), we focused on Tms and Tregs. In both subsets, the percentages of G_2M cells in $p24^-$ cells of WT HIV-1-infected and HIV-1*Δvpr*-infected mice were similar to those of mock-infected mice (Figure 5B). In contrast, we detected a significant level of $p24^+$ cells at the G_2M phase in Tms and Tregs (Figure 5B). Of note, the percentage of G_2M cells in $p24^+$ Tregs of WT HIV-1-infected mice reached a maximum of 37.1±2.8% and was significantly higher than that of HIV-1*Δvpr*-infected mice (Figure 5B). These results suggested that the level of Vpr-mediated G_2 arrest was the highest in HIV-1-infected Tregs.

Since it has been suggested that the G_2 arrest in HIV-1-infected cells results in the augmentation of virus production [3,35], we next focused on the relationship between the HIV-1 production potential and cell cycle condition in Tms and Tregs. Figure 5C illustrated that G_2M cells displayed higher percentages of p24-positive cells than G_0G_1 cells in both Tm and Treg. Surprisingly, 74.1±5.4% of Tregs at the G_2M phase in WT HIV-1-infected mice were positive for p24 (Figure 5C, left and right panels), and the p24 MFI in $p24^+$ Tregs at G_2M phase was highest (Figure 5C, middle and right panels). Taken together, these findings suggested that the majority of Tregs were infected with HIV-1 and arrested at the G_2 phase by Vpr, resulting in the augmentation of HIV-1 production during acute infection.

Vpr directly induces apoptosis in infected Tregs associated with G_2 cell cycle arrest

In addition to the augmentation of viral replication by Vpr, we also observed a severe depletion of Tregs in R5 WT HIV-1-infected humanized mice (Figure 2A–2D). It is known that Vpr can induce apoptosis through a caspase 3/8 (CASP3/8)-dependent pathway [1]. Therefore, we next analyzed the level of active CASP3, which is a direct inducer of apoptosis, in infected humanized mice. In the population of p24-negative cells, we found a significant increase of active $CASP3^+$ cells in WT HIV-1-infected mice (Figure 6A). Additionally, in both WT HIV-1-infected and HIV-1*Δvpr*-infected mice, the percentage of active CASP3 in $p24^+$ cells was significantly higher than that in $p24^-$ cells, yet the percentage of active CASP3 in $p24^+$ cells of WT HIV-1-infected cells was significantly higher than that of HIV-1*Δvpr*-infected mice (Figure 6A).

We then evaluated the magnitude of apoptosis in each $CD4^+$ T cell subset. As shown in Figure 6B, the percentage of active $CASP3^+$ cells in $p24^-$ Tms and Tregs of WT HIV-1-infected mice significantly increased when compared with those of mock-infected mice. On the other hand, the percentage of active $CASP3^+$ cells was significantly increased in $p24^+$ cells and was highest in $p24^+$ Tregs of WT HIV-1-infected mice (26.6±3.9%; Figure 6B), suggesting that Tregs are highly sensitive to Vpr-mediated apoptosis.

In addition to the apoptosis directly induced by Vpr, accumulating evidence has suggested a role for innate immune activation, including NK cells, in the $CD4^+$ T cell depletion after primary HIV-1 infection in individuals [36,37]. Also, it has been recently reported that Vpr upregulates the surface expression of some NK receptor ligands, such as UL16 binding protein 2

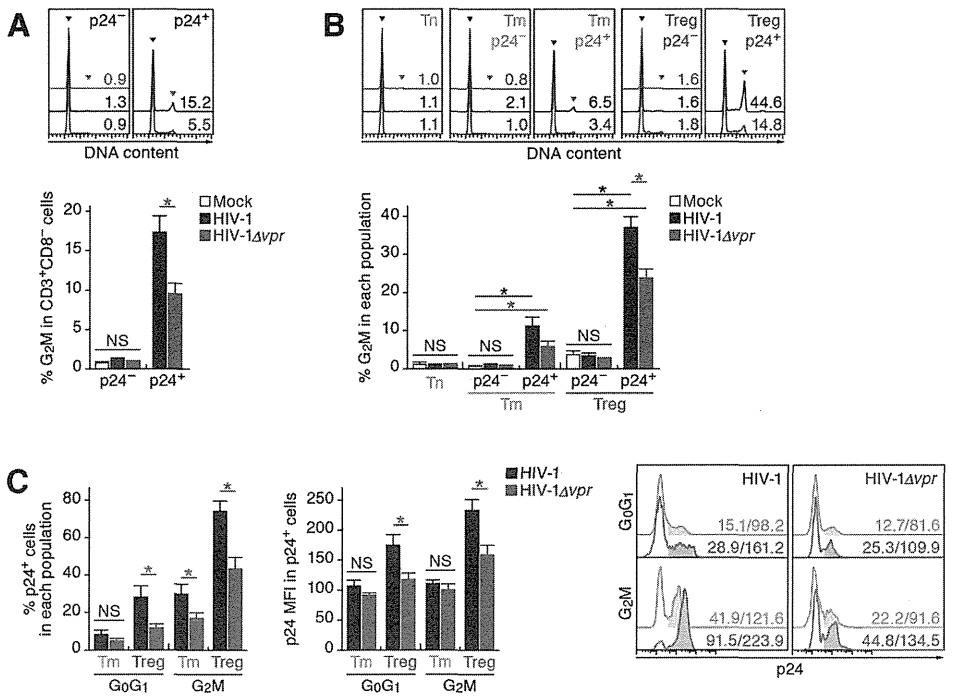

Figure 5. Effect of Vpr on G_2 cell cycle arrest in infected humanized mice. Splenic MNCs of WT HIV-1-infected mice (n = 12), *vpr*-deficient HIV-1-infected mice (n = 11), and mock-infected mice (n = 15) at 7 dpi were analyzed by flow cytometry using Hoechst33342 and an anti-HIV-1 p24 antibody. (A and B) The percentages of G_2M cells in $CD3^+$ $CD8^-$ cells (A) and in each population (B) are shown, respectively. Representative histograms are shown on the right panel. The black arrowhead indicates the peak of G_0G_1 cells, and the red arrowhead indicates the peak of G_2M cells. The numbers in the histogram indicate the percentage of G_2M cells in each population. (C) The percentage of $p24^+$ cells in each population (left) and the MFI of p24 in $p24^+$ cells of each population (middle). Representative histograms are respectively shown. The numbers in the histogram indicate the percentage of positive cells (left) and MFI values (right). Statistical differences were determined by Welch's *t* test, and statistically significant differences ($P<0.05$) are shown as follows: mock versus WT HIV-1, black asterisk; mock versus HIV-1*Δvpr*, blue asterisk; and WT HIV-1 versus HIV-1*Δvpr*, red asterisk. NS, no statistical significance. Data represent mean ± SEM.
doi:10.1371/journal.ppat.1003812.g005

(ULBP2), which leads to NK cell-dependent cell death [38,39]. These reports led to the hypothesis that Vpr upregulates the expression level of ULBP2 on HIV-1-infected Tregs and enhances NK cell-dependent cell death. To address this possibility, we assessed the expression level of ULBP2 in infected humanized mice. However, the expression level of ULBP2 on the surface of WT HIV-1-infected cells was comparable to those of HIV-1*Δvpr*-infected cells, uninfected cells, and the $CD4^+$ T cells in mock-infected mice (Figure S4). Taken together, these results suggested that the decrease of Tregs in R5 WT HIV-1-infected mice was not dependent on the NK cell-dependent cell death but due to Vpr expressed in infected cells.

In order to investigate the relationship between G_2 cell cycle arrest and apoptosis, both of which are mediated by Vpr, we performed p24 staining in combination with Hoechst and active CASP3 staining. In each $CD4^+$ T cell subset positive for p24, the percentage of active $CASP3^+$ cells at G_2M was significantly higher than that at the G_0G_1 phase (Figure 6C). Moreover, the percentage of active $CASP3^+$ cells was highest in $p24^+$ Tregs at G_2M in WT HIV-1-infected mice (35.9±5.4%; Figure 6C), strongly suggesting that Vpr-mediated apoptosis was most efficiently induced in infected Tregs arrested at the G_2 phase.

Treg depletion can trigger immune activation and augmented HIV-1 propagation *in vivo*

The aforementioned findings suggested that Vpr promotes R5 HIV-1 propagation during the acute phase of infection by exploiting proliferating $CCR5^+$ $CD4^+$ T cells including Tregs *in vivo*. In addition, Vpr is associated with the rapid decrease of Tregs, leading to immune activation. Since it is known that HIV-1 replicates more efficiently in activated $CD4^+$ T cells than non-activated $CD4^+$ T cells [40,41], our findings suggested that the immune activation induced by Vpr-mediated Treg depletion led to the augmented viral propagation *in vivo*. To address this possibility, denileukin diftitox (DD), which is known to specifically target and deplete Tregs, was intraperitoneally treated into humanized mice. As shown in Figure 7A and 7B, Tregs were specifically and significantly depleted by treatment with DD for 3 days, while the cell numbers of the other populations such as $CD45^+$ human white blood cells, total $CD4^+$ T cells, Tns, and Tms did not change significantly. We also found that the Treg depletion by DD induced immune activation and proliferation of splenic memory $CD8^+$ T cells (Figure 7C). Interestingly, the percentage of $MKI67^+$ cells in the Tms of DD-treated humanized mice was significantly higher than those in Tms and Tregs of untreated humanized mice (Figure 7D). In addition, the levels of CCR5 on Tms and Tns in DD-treated mice were significantly higher than that in untreated mice (Figure 7E), suggesting that the population size of proliferating $CCR5^+$ $CD4^+$ T cells in DD-treated humanized mice is greater than that in untreated humanized mice.

R5 WT and *vpr*-deficient HIV-1 (strain JR-CSF) were then inoculated into 13 DD-treated humanized mice, respectively. As shown in Figure 7F, the number of $CD4^+$ T cells, particularly Tms, in the PB of DD-treated uninfected mice gradually increased, while that those of DD-treated WT and *vpr*-deficient

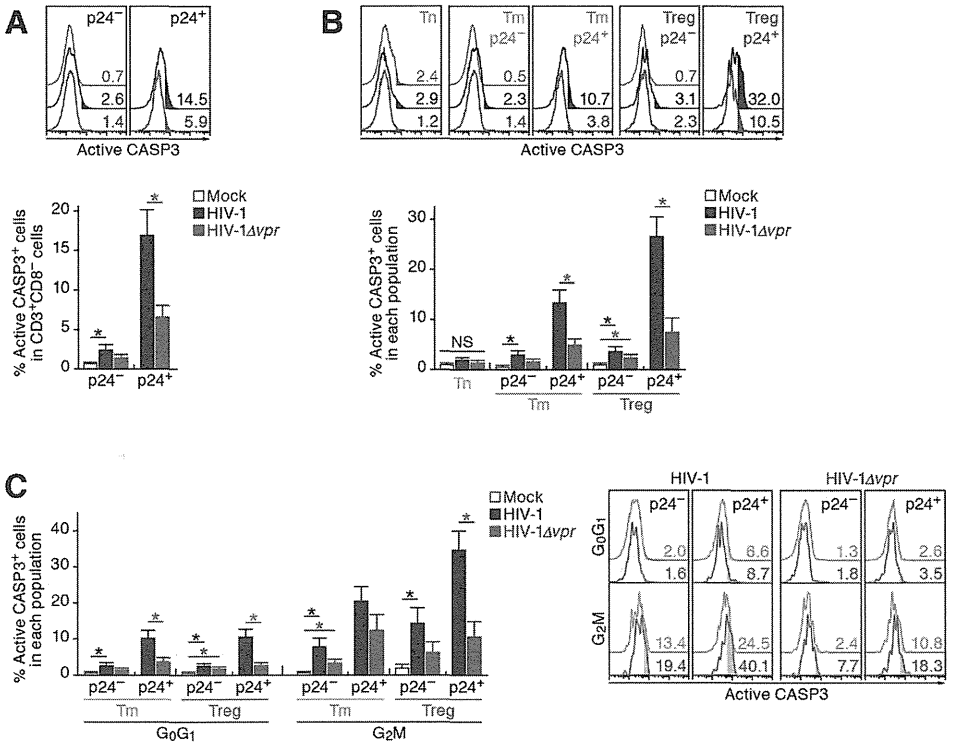

Figure 6. Effect of Vpr on apoptosis and its relevance in G_2 cell cycle arrest in infected humanized mice. Splenic MNCs of WT HIV-1-infected mice (n = 7), *vpr*-deficient HIV-1-infected mice (n = 7), and mock-infected mice (n = 9) at 7 dpi were analyzed by flow cytometry using anti-active CASP3 and anti-HIV-1 p24 antibodies without (A and B) or with (C) or Hoechst33342. (A and B) Effect of Vpr on apoptosis. The percentages of active CASP3$^+$ cells in CD3$^+$ CD8$^-$ cells (A) and in each population (B) are shown, respectively. Representative histograms are shown on the right panel. The numbers in the histogram indicate the percentage of active CASP3$^+$ cells in each population. (C) Relevance between G_2 arrest and apoptosis. The percentage of active CASP3$^+$ cells in each population is shown. Representative histograms are respectively shown. The numbers in the histogram indicate the percentage of active CASP3$^+$ cells in each population. Statistical differences were determined by Welch's *t* test, and statistically significant differences ($P<0.05$) are shown as follows: mock versus WT HIV-1, black asterisk; mock versus HIV-1*Δvpr*, blue asterisk; and WT HIV-1 versus HIV-1*Δvpr*, red asterisk. NS, no statistical significance. Data represent mean ± SEM.
doi:10.1371/journal.ppat.1003812.g006

HIV-1 infected mice severely decreased after 7 dpi. We also observed a gradual increase of memory CD8$^+$ T cells in the PB of DD-treated humanized mice regardless of HIV-1 infection (Figure S5). It was of particular importance that rapid and massive HIV-1 replication in DD-treated mice compared with untreated mice infected with either virus, and that the viral load in DD-treated WT HIV-1-infected mice was significantly higher than that in DD-treated HIV-1*Δvpr*-infected mice at 4 and 7 dpi (Figure 7G). Furthermore, the slope of virus growth in DD-treated WT HIV-1-infected mice was significantly higher than those of DD-treated HIV-1*Δvpr*-infected mice and untreated WT HIV-1-infected mice (Figure 7H). Taken together, these findings suggest that R5 HIV-1 massively propagates under an activated condition, and that Vpr enhances viral expansion in CCR5$^+$ proliferating CD4$^+$ T cell population.

Discussion

The fact that *vpr* is conserved in transmitted/founder viruses in infected individuals [42] may indicate its importance during the acute phase of HIV-1 propagation. However, even though there is abundant evidence of Vpr's roles in G_2 arrest and apoptosis *in vitro* [1,43,44], its impact on for HIV-1 replication *in vivo* remains unclear. In this study, we demonstrated that Vpr augments R5 HIV-1 propagation by exploiting proliferating CCR5$^+$ CD4$^+$ T cells including Tregs during acute infection. We also observed significant levels of Vpr-dependent G_2 arrest and apoptosis in R5 HIV-1-infected Tregs, which may result in the Treg depletion and subsequent immune activation. This is the first report to directly demonstrate that Vpr positively affects HIV-1 replication by taking advantage of Tregs *in vivo*.

A previous study has demonstrated that Tregs highly express CCR5, correlating with their high susceptibility to R5 HIV-1 *in vitro* [15]. Here, by using a humanized mouse model, we demonstrated that Tregs express higher level of CCR5 (Figure 1) and are highly susceptible to R5 HIV-1 infection *in vivo* (Figure 3). In addition, it is well known that HIV-1 replicates more efficiently in activated/proliferating cells than in non-activated cells [40,41]. Consistent with previous reports [9–11], we showed that Tregs are highly proliferative *in vivo* when compared with the other CD4$^+$ T cell subsets such as Tns and Tms (Figure 1). Therefore, it is reasonable to assume that R5 HIV-1 efficiently replicates in Tregs of humanized mice because of their higher CCR5 expression level and higher proliferating status. Moreover, in line with the previous observations that Vpr arrests the cell cycle of HIV-1-infected cells at G_2 phase where LTR-driven HIV-1 transcription is most active [3,35], we found that the MFI of p24, which reflects the expression level of viral proteins, in Tregs of WT HIV-1-infected mice was ~2-fold higher than that of HIV-1*Δvpr*-infected mice, while expression levels in Tns and Tms were comparable between WT and *vpr*-deficient HIV-1 (Figure 3C). Furthermore, we revealed that Vpr-dependent G_2

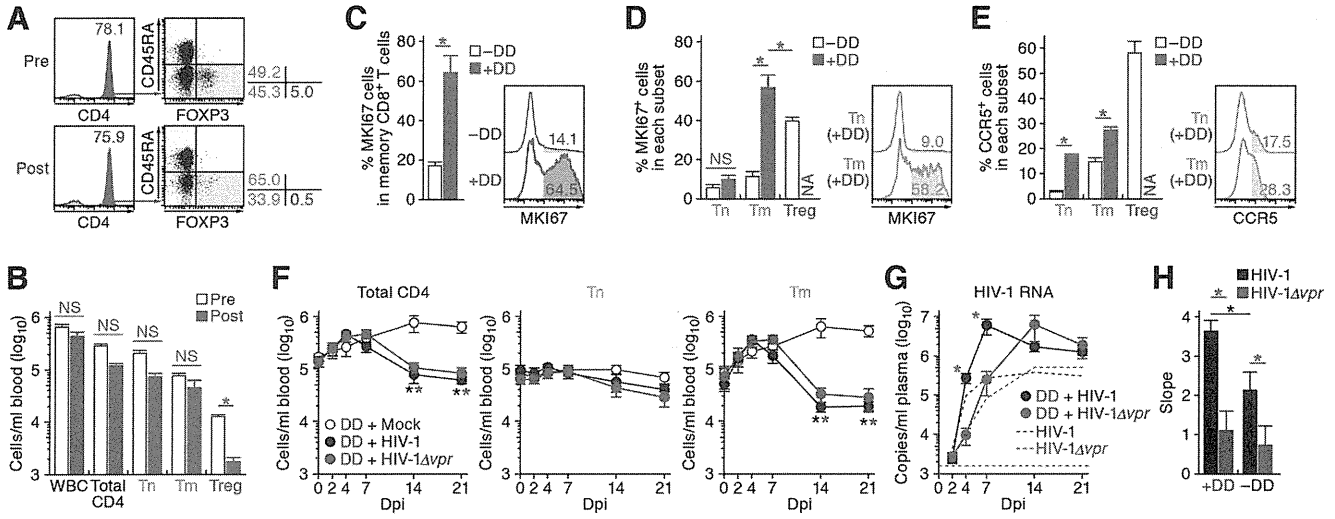

Figure 7. Augmentation of Vpr's effect and HIV-1 propagation by Treg depletion. (A to D) Evaluation of Treg depletion by treatment with DD. DD was administrated into humanized mice (n = 14) as described in Materials and Methods. (A and B) Specific depletion of Tregs by treatment with DD. The levels of human white blood cells (WBC; $CD45^+$ cells) and $CD4^+$ T cell subsets in PB of humanized mice before and after the DD treatment for 3 days were compared. Representatives (A) and the numbers of each human leukocytes in PB (B) are shown. In panel A, the numbers in the histogram indicate the percentage of $CD4^+$ cells in $CD45^+$ $CD3^+$ cells, and the numbers on the right of the dot plots indicate the percentage of the cells in each quadrant. (C and D) Immune activation by treatment with DD. The percentages of $MKI67^+$ cells in memory $CD8^+$ T cells (C) and in each $CD4^+$ T cell subset (D) in the spleen of humanized mice treated with (n = 5) or without (n = 8) DD for 7 days are shown, respectively. (E) Up-regulation of CCR5 expression by DD treatment. The percentage of $CCR5^+$ cells in each $CD4^+$ T cell subset in the spleen of humanized mice treated with (n = 5) or without (n = 8) DD for 7 days is shown. In panels C to E, the numbers in the histogram indicate positivity. (F to H) Dynamics of HIV-1 infection in DD-treated humanized mice. (F) The numbers of peripheral $CD4^+$ T cells, Tns, Tms, and Tregs (F) and the amounts of viral RNA in the plasma (G) of R5 WT HIV-1-infected DD-treated mice (n = 13), R5 *vpr*-deficient HIV-1-infected DD-treated mice (n = 13), and mock-infected DD-treated mice (n = 8) were routinely quantified as described in the legends of Figure 2A and 3A, respectively. In panel G, the broken black and blue lines indicate the averages of WT HIV-1-infected mice (n = 30) and *vpr*-deficient HIV-1-infected mice (n = 23) without DD treatment, which corresponds to the results shown in Figure 3A. The horizontal broken line indicates the detection limit of the assay (1,600 copies/ml). (H) Kinetics of viral expansion. The slopes of the amounts of viral RNA in the plasma of WT HIV-1-infected DD-treated mice (n = 13), *vpr*-deficient HIV-1-infected DD-treated mice (n = 13), WT HIV-1-infected mice (n = 30) and *vpr*-deficient HIV-1-infected mice (n = 23) until 7 dpi are shown. Statistical difference was determined by Welch's *t* test. In panels B to E, statistically significant differences ($P<0.05$) are indicated by red asterisks. In panels F and G, statistically significant differences ($P<0.05$) are shown as follows: mock versus WT HIV-1, black asterisk; mock versus HIV-1*Δvpr*, blue asterisk; and WT HIV-1 versus HIV-1*Δvpr*, red asterisk. In panel H, statistically significant differences ($P<0.05$) are shown as follows: with and without DD treatment, black asterisk; and WT HIV-1 versus HIV-1*Δvpr*, red asterisk. NS, no statistical significance. Data represent mean ± SEM. NA, not analyzed.
doi:10.1371/journal.ppat.1003812.g007

cell cycle arrest was efficiently occurred in infected Tregs (Figure 5B), and that both the percentage $p24^+$ cells and the p24 MFI was highest in WT HIV-1-infected Tregs at G_2 phase (Figure 5C). Taken together, these findings strongly suggest that Vpr promotes R5 HIV-1 replication during acute infection by increasing the viral production in Tregs.

In contrast to the findings in R5 HIV-1-infected humanized mouse model, we observed neither the acceleration of virus replication by Vpr during the acute phase of HIV-1 infection (Figure 4C), nor the Treg depletion (Figure 4D–4F), nor subsequent immune activation (Figure 4G) in X4 HIV-1-infected humanized mice. In Tregs, CCR5 is predominantly expressed (Figure 1C and 1D), whereas CXCR4 is broadly expressed in all $CD4^+$ T cell subsets (Figure 4A and 4B), which is consistent with previous findings [15,28]. Therefore, these results suggest that the Vpr-dependent augmentation of HIV-1 replication during acute infection is dependent on viral tropism and is restricted to R5 HIV-1. Regarding HIV-1 tropism, it is of particular importance that R5 HIV-1 is the major clinical isolates from patients, along with transmitted/founder viruses [42,45,46], while X4 HIV-1 occasionally emerges during the onset of AIDS [47,48]. Therefore, the findings in R5 HIV-1-infected humanized mice more properly reflect those in patients than those in X4 HIV-1-infected mice, and the role of Vpr in R5 HIV-1-infected humanized mice is physiologically more relevant.

The concept that Vpr augments R5 HIV-1 replication by utilizing proliferating $CCR5^+$ $CD4^+$ T cells is further supported by the DD treatment experiments (Figure 7): the human leukocytes including Tms in the mice treated with DD were highly proliferative and the Tms in DD-treated mice expressed higher level of CCR5. Moreover, R5 HIV-1 propagated more efficiently when compared with the untreated mice. Interestingly, it has been reported that Vpr enhances HIV-1 LTR-driven transcription in cycling $CD4^+$ T cells but not in non-cycling cells [3]. Taken together, these findings suggest that Vpr-dependent promotion of R5 HIV-1 production during acute infection is attributed to the target cell tropism of HIV-1 and the activated/proliferative status of the target cells.

There is a longstanding dogma that the immune activation caused by HIV-1/SIV infection closely associates with the disease progression [49]. Regarding the triggering of immune activation, previous studies have suggested that the immune activation in HIV-1-infected individuals and SIV-infected monkeys can be caused by (1) massive infection and loss of $CD4^+$ T cells [50,51]; (2) inflammatory cytokines [52,53]; and (3) microbial translocation from the luminal intestinal tract [54]. In this study, Treg depletion and immune activation were observed in R5 but not X4 HIV-1-infected humanized mice (Figure 2 and 4). These findings are consistent with previous observations in HIV-1-infected patients [15–17], SIV-infected monkeys [18–20], and a CCR5/CXCR4

dual-tropic HIV-1-infected humanized mouse model [28]. Particularly noteworthy is that *vpr*-deficient HIV-1-infected humanized mice showed neither Treg depletion nor immune activation. These findings raise a possibility that Vpr is associated with the induction of immune activation by depleting Tregs. Since the physiological role of Tregs *in vivo* is to suppress excessive immune activation [7], it is conceivable that Vpr-mediated Treg depletion can be one of the triggers for immune activation in HIV-1-infected individuals. However, the mechanism of the immune activation by HIV-1/SIV infection still remains unsolved for more than two decades of intense research, and there are lines of other possibilities such as the activation of dendritic cells/macrophages due to higher number of cell death [55–57] and the actual depletion of myeloid-derived suppressor cells [58,59] by direct or indirect virus infection. Although our results suggest that Vpr is associated with the acute Treg depletion and subsequent immune activation in R5 HIV-1-infected humanized mice, further investigations is necessary to elucidate the mechanisms of the immune activation by HIV-1/SIV infection.

In DD-treated humanized mice, we observed the activation/proliferation (Figure 7C) and the expansion (Figure S5) of memory $CD8^+$ T cells. As a previous report using R5 HIV-1-infected humanized mice showed that the depletion of $CD8^+$ T cells accelerates HIV-1 replication [60], these findings raise a possibility that the expanded memory $CD8^+$ T cells restrict HIV-1 replication in DD-treated humanized mice. However, the previous study [60] depleted $CD8^+$ T cells in R5 HIV-1-infected humanized mice during chronic infection (i.e, 5–7 weeks postinfection) and observed the increase of virus growth 2 weeks after $CD8^+$ T cell depletion. On the other hand, although the increase of memory $CD8^+$ T cells was observed in DD-treated humanized mice after 4 or 7 dpi (Figure S5), here we particularly focused on the dynamics of HIV-1 infection during the acute phase (i.e., until 7 dpi) and observed a sharp increase of HIV-1 replication in DD-treated mice prior to the expansion of memory $CD8^+$ T cells (Figure 7G). Moreover, the activation and expansion of $CD8^+$ T cells were detected in DD-treated humanized mice regardless of HIV-1 infection, strongly suggesting that this $CD8^+$ T cell expansion is not triggered by HIV-1 infection but by the DD-mediated Treg depletion. Furthermore, although the expansion of memory $CD8^+$ T cells during chronic infection has been observed in certain HIV-1-infected human HSC-transplanted humanized mouse models [61–63] including ours [25], it is controversial whether or not the human $CD8^+$ T cells differentiated in human HSC-transplanted humanized mouse models possess the potential to efficiently elicit acquired immune responses against pathogens including HIV-1 [64–66]. These findings suggest that the expanded $CD8^+$ T cells in DD-treated humanized mice have smaller effect on the virus growth during the acute phase of HIV-1 infection.

Soluble Vpr proteins are secreted from infected cells and can be detected in patient sera [67,68]. In p24-negative cells of WT HIV-1-infected mice, we found a significant level of apoptosis (Figure 6A and 6B), while G_2 arrest was not observed (Figure 5A and 5B). These results suggest that soluble Vpr can trigger apoptosis but not G_2 arrest in bystander cells. In fact, it was reported that the Vpr expressed in HIV-1-infected cells robustly induce both G_2 arrest and apoptosis, while soluble Vpr secreted from HIV-1-infected cells can induce apoptosis but not G_2 arrest [69]. However, in addition to WT HIV-1-infected cells, G_2 arrest was also partially observed in HIV-1*Δvpr*-infected cells (Figure 5A and 5B). In this regard, it has been reported that another accessory protein of HIV-1, Vif, is also able to cause G_2 arrest in a Vpr-independent manner [70–72], strongly suggesting that the G_2 arrest in HIV-1*Δvpr*-infected cells is induced by Vif. Although the significance of functional redundancy of Vpr and Vif for G_2 arrest remains unclear, further studies using humanized mice will reveal their impact.

In summary, we demonstrated for the first time that one of the major roles of Vpr in HIV-1 infection and pathogenesis is to enhance R5 HIV-1 propagation by exploiting proliferating $CCR5^+$ $CD4^+$ T cells including Tregs during acute infection, which can subsequently induce immune activation. Our findings suggest that the action of Vpr *in vivo* may provide HIV-1 with an optical condition to replicate and facilitate HIV-1 expansion *in vivo*.

Materials and Methods

Ethics statement

All procedures including animal studies were conducted following the guidelines for the Care and Use of Laboratory Animals of the Ministry of Education, Culture, Sports, Science and Technology, Japan. These studies were approved by the Institutional Animal Care and Use Committees (IACUC)/ethics committee of Kyoto University (protocol number D13–25). All protocols involving human subjects were reviewed and approved by the Kyoto University institutional review board. Informed written consent from human subjects was obtained in this study.

Humanized mice

NOD.Cg-*Prkdc*^{scid} *Il2rg*^{tm1Sug}/*Jic* (NOD/SCID *Il2rg*$^{-/-}$) mice [73] were obtained from the Central Institute for Experimental Animals (Kawasaki, Kanagawa, Japan). The mice were maintained under specific-pathogen-free conditions and were handled in accordance with the regulations of the IACUC/ethics committee of Kyoto University. Human $CD34^+$ HSCs were isolated from human fetal liver as described previously [74]. The humanized mouse (NOG-hCD34 mouse) was constructed as previously described [21–24]. Briefly, 164 newborn (aged 0 to 2 days) NOG mice from 38 litters were irradiated with X-ray (10 cGy per mouse) by an RX-650 X-ray cabinet system (Faxitron X-ray Corporation) and were then intrahepatically injected with the obtained human fetal liver-derived $CD34^+$ cells (7.5×10^4 to 25×10^4 cells). A list of the humanized mice used in this study is summarized in Table S1.

Virus preparation and infection

Virus solutions of R5 WT HIV-$1_{JR\text{-}CSF}$ [30], R5 *vpr*-deficient HIV-$1_{JR\text{-}CSF}$ [33], X4 WT HIV-$1_{NL4\text{-}3}$ [34], and X4 *vpr*-deficient HIV-$1_{NL4\text{-}3}$ [2] were prepared and titrated as previously described [23]. Virus solutions of 10^5 50% tissue culture infectious doses ($TCID_{50}$) were intraperitoneally inoculated into NOG-hCD34 mice. RPMI 1640 was used for mock infection.

HIV-1 RNA quantification, TZM-bl assay, and western blotting

The amount of HIV-1 RNA in plasma was quantified by Bio Medical Laboratories, Inc. TZM-bl assay and Western blotting were performed as previously described [22,23]. For Western blotting, mouse anti-Vpr antibody (clone 8D1) [68] and goat anti-p24 antiserum (ViroStat) were used.

PB collection and isolation of splenic mononuclear cells

PB and plasma were routinely collected as previously described [21–24]. Splenic human mononuclear cells (MNCs) were isolated as previously described [22–24].

Flow cytometry and hematocytometry

Flow cytometry was performed with FACSCanto (BD Biosceiences) as previously described [21–24]. Hematocytometry was performed with Celltac alpha MEK-6450 (Nihon Kohden Co) as previously described [23,24]. Briefly, 10 μl of the PB of humanized mice were used for hematometry, and the number of MNCs per microliter was measured. The antibodies used in flow cytometry analysis are listed in Table S2. For cell cycle analysis, cellular DNA was stained with Hoechst33342 (Invitrogen) as previously described [21], and DNA contents were analyzed by using ModFit LT software (Verify software house) according to the manufacture's protocol and as previously reported [72]. For the measurement of the level of apoptosis, anti-active CASP3 antibody conjugated with PE (BD Biosciences; Table S2) was used according to the manufacture's procedure.

Denileukin diftitox treatment for Treg depletion

Denileukin diftitox (DD; IL-2 conjugated with diphtheria toxin) were purchased from Ligand Pharma, Co. For Treg depletion in humanized mice, DD (400 μg/200 μl in PBS) were intraperitoneally treated once per day. For HIV-1 infection following DD treatment, the humanized mice treated with DD for 3 days were intraperitoneally inoculated with virus solutions of 10^5 $TCID_{50}$. RPMI 1640 was used as the mock infection. To maintain Treg depletion following virus inoculation, DD was intraperitoneally treated once per day.

Statistical analyses

Data were expressed as averages with SEMs. Significant differences ($P<0.05$) were determined by Welch's *t* test or Student's *t* test.

Accession numbers

SwissProt (http://www.uniprot.org/) or GenBank (http://www.ncbi.nlm.nih.gov/genbank) accession numbers for the proteins mentioned in the text are as follows: CD3 (P07766); CD4 (P01730); CD8 (NP_001759.3); CD25 (NP_000408.1); CD38 (P28907); CD45 (NP_002829.3); CD45RA (P08575); CD127 (P16871); CASP3 (P42574); CCR5 (P51681); CXCR4 (P61073); CTLA4 (P16410); FOXP3 (Q9BZS1); MKI67 (P46013); ULBP2 (Q9BZM5). These proteins were detected by flow cytometry using the antibodies listed in Table S2. The accession numbers from GenBank (http://www.ncbi.nlm.nih.gov/genbank) for the viruses mentioned in the text are as follows: HIV-1 strain JR-CSF (M38429.1); HIV-1 strain NL4-3 (M19921.2).

Supporting Information

Figure S1 Depletion of Treg by WT HIV-1 infection. The percentage of $FOXP3^+$ $CD4^-$ cells in splenic MNCs of WT HIV-1-infected mice (n = 5) and mock-infected mice (n = 5) at 21 dpi are shown. Representative dot plots are shown below. The numbers under the dot plots correspond to the percentage in each quadrant. NS, no statistical significance.
(TIF)

Figure S2 Infectivity of R5 WT and *vpr*-deficient HIV-1. R5 WT and *vpr*-deficient HIV-1 (strain JR-CSF) were prepared as described in Materials and Methods. (Top) Western blot analyses of the virions. (Bottom) TZM-bl assay. Prepared virus solutions were inoculated into TZM-bl indicator cells. The infectivities of these viruses were quantified as described in Materials and Methods and were normalized to the amount of p24. The assay was performed in triplicate. NS, no statistical significance.
(TIF)

Figure S3 Infectivity of X4 WT and *vpr*-deficient HIV-1. X4 WT and *vpr*-deficient HIV-1 (strain NL4-3) were prepared as described in Materials and Methods. (Top) Western blot analyses of the virions. (Bottom) TZM-bl assay. Prepared virus solutions were inoculated into TZM-bl indicator cells. The infectivities of these viruses were quantified as described in Materials and Methods and were normalized to the amount of p24. The assay was performed in triplicate. NS, no statistical significance.
(TIF)

Figure S4 No association of ULBP2 with the Treg depletion observed in WT HIV-1-infected mice. Splenic MNCs of WT HIV-1-infected mice (n = 7), *vpr*-deficient HIV-1-infected mice (n = 7), and mock-infected mice (n = 7) at 7 dpi were analyzed by flow cytometry using an anti-ULBP2 and an anti-HIV-1 p24 antibodies. The percentages of $ULBP2^+$ cells in $CD3^+$ $CD8^-$ cells (A) and in each population (B) are respectively shown. Representative histograms are shown on the right. The numbers in histogram indicate the percentage of active $CASP3^+$ cells in each population. Statistical difference was determined by Welch's *t* test. NS, no statistical significance.
(TIF)

Figure S5 Expansion of memory $CD8^+$ T cells in DD-treated humanized mice. The numbers of total $CD8^+$ T cells ($CD45^+$ $CD3^+$ $CD8^+$ cells), naïve $CD8^+$ T cells ($CD45^+$ $CD3^+$ $CD8^+$ $CD45RA^+$ cells), and memory $CD8^+$ T cells ($CD45^+$ $CD3^+$ $CD8^+$ $CD45RA^-$ cells) in the PB of R5 WT HIV-1-infected DD-treated mice (n = 13), R5 *vpr*-deficient HIV-1-infected DD-treated mice (n = 13), and mock-infected DD-treated mice (n = 8) were routinely quantified by flow cytometry and hematocytometry.
(TIF)

Table S1 Humanized mice used in this study. A full list of the 132 humanized mice used in this study.
(PDF)

Table S2 Antibodies used in flow cytometry analyses. A full list of antibodies used in this study.
(PDF)

Acknowledgments

We would like to thank Peter Gee (Institute for Virus Research, Kyoto University, Japan) and Keiko Okano (Research Administration Office, Kyoto University, Japan) for proofreading this manuscript, Yoshinori Fukazawa (Oregon Health and Science University, United States of America), Rob J. de Boer (Utrecht University, the Netherland), Shimon Sakaguchi, and Motonao Osaki (Institute for Medical Sciences, Kyoto University, Japan) for helpful suggestions and discussion, and Yuetsu Tanaka (University of the Ryukyus, Japan) and Akio Adachi (The University of Tokushima) for providing materials. We also thank all the members in the laboratory of Virus Pathogenesis, Institute for Virus Research, Kyoto University for lively discussion and Kotubu Misawa for the dedicated support.

Author Contributions

Conceived and designed the experiments: KS YK. Performed the experiments: KS NM YS. Analyzed the data: KS NM SI YS MM. Contributed reagents/materials/analysis tools: SI MM YI MI KA DSA. Wrote the paper: KS YK.

References

1. Andersen JL, Le Rouzic E, Planelles V (2008) HIV-1 Vpr: mechanisms of G2 arrest and apoptosis. Exp Mol Pathol 85: 2–10.
2. Ogawa K, Shibata R, Kiyomasu T, Higuchi I, Kishida Y, et al. (1989) Mutational analysis of the human immunodeficiency virus *vpr* open reading frame. J Virol 63: 4110–4114.
3. Gummuluru S, Emerman M (1999) Cell cycle- and Vpr-mediated regulation of human immunodeficiency virus type 1 expression in primary and transformed T-cell lines. J Virol 73: 5422–5430.
4. Eckstein DA, Sherman MP, Penn ML, Chin PS, De Noronha CM, et al. (2001) HIV-1 Vpr enhances viral burden by facilitating infection of tissue macrophages but not nondividing $CD4^+$ T cells. J Exp Med 194: 1407–1419.
5. Hoch J, Lang SM, Weeger M, Stahl-Hennig C, Coulibaly C, et al. (1995) *vpr* deletion mutant of simian immunodeficiency virus induces AIDS in rhesus monkeys. J Virol 69: 4807–4813.
6. Stevenson M (2003) HIV-1 pathogenesis. Nat Med 9: 853–860.
7. Sakaguchi S, Miyara M, Costantino CM, Hafler DA (2010) $FOXP3^+$ regulatory T cells in the human immune system. Nat Rev Immunol 10: 490–500.
8. Hori S, Nomura T, Sakaguchi S (2003) Control of regulatory T cell development by the transcription factor Foxp3. Science 299: 1057–1061.
9. Fisson S, Darrasse-Jeze G, Litvinova E, Septier F, Klatzmann D, et al. (2003) Continuous activation of autoreactive $CD4^+CD25^+$ regulatory T cells in the steady state. J Exp Med 198: 737–746.
10. Vukmanovic-Stejic M, Zhang Y, Cook JE, Fletcher JM, McQuaid A, et al. (2006) Human $CD4^+CD25^{hi}Foxp3^+$ regulatory T cells are derived by rapid turnover of memory populations in vivo. J Clin Invest 116: 2423–2433.
11. Miyara M, Yoshioka Y, Kitoh A, Shima T, Wing K, et al. (2009) Functional delineation and differentiation dynamics of human $CD4^+$ T cells expressing the FoxP3 transcription factor. Immunity 30: 899–911.
12. Dittmer U, He H, Messer RJ, Schimmer S, Olbrich AR, et al. (2004) Functional impairment of $CD8^+$ T cells by regulatory T cells during persistent retroviral infection. Immunity 20: 293–303.
13. Weiss L, Donkova-Petrini V, Caccavelli L, Balbo M, Carbonneil C, et al. (2004) Human immunodeficiency virus-driven expansion of $CD4^+CD25^+$ regulatory T cells, which suppress HIV-specific CD4 T-cell responses in HIV-infected patients. Blood 104: 3249–3256.
14. Holmes D, Jiang Q, Zhang L, Su L (2008) Foxp3 and Treg cells in HIV-1 infection and immuno-pathogenesis. Immunol Res 41: 248–266.
15. Oswald-Richter K, Grill SM, Shariat N, Leelawong M, Sundrud MS, et al. (2004) HIV infection of naturally occurring and genetically reprogrammed human regulatory T-cells. PLoS Biol 2: E198.
16. Apoil PA, Puissant B, Roubinet F, Abbal M, Massip P, et al. (2005) FOXP3 mRNA levels are decreased in peripheral blood $CD4^+$ lymphocytes from HIV-positive patients. J Acquir Immune Defic Syndr 39: 381–385.
17. Eggena MP, Barugahare B, Jones N, Okello M, Mutalya S, et al. (2005) Depletion of regulatory T cells in HIV infection is associated with immune activation. J Immunol 174: 4407–4414.
18. Pereira LE, Villinger F, Onlamoon N, Bryan P, Cardona A, et al. (2007) Simian immunodeficiency virus (SIV) infection influences the level and function of regulatory T cells in SIV-infected rhesus macaques but not SIV-infected sooty mangabeys. J Virol 81: 4445–4456.
19. Chase AJ, Yang HC, Zhang H, Blankson JN, Siliciano RF (2008) Preservation of $FoxP3^+$ regulatory T cells in the peripheral blood of human immunodeficiency virus type 1-infected elite suppressors correlates with low $CD4^+$ T-cell activation. J Virol 82: 8307–8315.
20. Favre D, Lederer S, Kanwar B, Ma ZM, Proll S, et al. (2009) Critical loss of the balance between Th17 and T regulatory cell populations in pathogenic SIV infection. PLoS Pathog 5: e1000295.
21. Nie C, Sato K, Misawa N, Kitayama H, Fujino H, et al. (2009) Selective infection of $CD4^+$ effector memory T lymphocytes leads to preferential depletion of memory T lymphocytes in R5 HIV-1-infected humanized NOD/SCID/IL-$2R\gamma^{null}$ mice. Virology 394: 64–72.
22. Sato K, Izumi T, Misawa N, Kobayashi T, Yamashita Y, et al. (2010) Remarkable lethal G-to-A mutations in *vif*-proficient HIV-1 provirus by individual APOBEC3 proteins in humanized mice. J Virol 84: 9546–9556.
23. Sato K, Misawa N, Fukuhara M, Iwami S, An DS, et al. (2012) Vpu augments the initial burst phase of HIV-1 propagation and downregulates BST2 and CD4 in humanized mice. J Virol 86: 5000–5013.
24. Sato K, Misawa N, Nie C, Satou Y, Iwakiri D, et al. (2011) A novel animal model of Epstein-Barr virus-associated hemophagocytic lymphohistiocytosis in humanized mice. Blood 117: 5663–5673.
25. Sato K, Nie C, Misawa N, Tanaka Y, Ito M, et al. (2010) Dynamics of memory and naive $CD8^+$ T lymphocytes in humanized NOD/SCID/IL-$2R\gamma^{null}$ mice infected with CCR5-tropic HIV-1. Vaccine 28 Suppl 2: B32–37.
26. Billerbeck E, Barry WT, Mu K, Dorner M, Rice CM, et al. (2011) Development of human $CD4^+FoxP3^+$ regulatory T cells in human stem cell factor-, granulocyte-macrophage colony-stimulating factor-, and interleukin-3-expressing NOD-SCID IL2Rγ^{null} humanized mice. Blood 117: 3076–3086.
27. Duan K, Zhang B, Zhang W, Zhao Y, Qu Y, et al. (2011) Efficient peripheral construction of functional human regulatory $CD4^+CD25^{high}Foxp3^+$ T cells in NOD/SCID mice grafted with fetal human thymus/liver tissues and $CD34^+$ cells. Transpl Immunol 25: 173–179.
28. Jiang Q, Zhang L, Wang R, Jeffrey J, Washburn ML, et al. (2008) $FoxP3^+CD4^+$ regulatory T cells play an important role in acute HIV-1 infection in humanized $Rag2^{-/-}\gamma C^{-/-}$ mice in vivo. Blood 112: 2858–2868.
29. Onoe T, Kalscheuer H, Danzl N, Chittenden M, Zhao G, et al. (2011) Human natural regulatory T cell development, suppressive function, and postthymic maturation in a humanized mouse model. J Immunol 187: 3895–3903.
30. Koyanagi Y, Miles S, Mitsuyasu RT, Merrill JE, Vinters HV, et al. (1987) Dual infection of the central nervous system by AIDS viruses with distinct cellular tropisms. Science 236: 819–822.
31. Bofill M, Mocroft A, Lipman M, Medina E, Borthwick NJ, et al. (1996) Increased numbers of primed activated $CD8^+CD38^+CD45RO^+$ T cells predict the decline of $CD4^+$ T cells in HIV-1-infected patients. AIDS 10: 827–834.
32. Benito JM, Lopez M, Lozano S, Martinez P, Gonzalez-Lahoz J, et al. (2004) CD38 expression on CD8 T lymphocytes as a marker of residual virus replication in chronically HIV-infected patients receiving antiretroviral therapy. AIDS Res Hum Retroviruses 20: 227–233.
33. Kawano Y, Tanaka Y, Misawa N, Tanaka R, Kira JI, et al. (1997) Mutational analysis of human immunodeficiency virus type 1 (HIV-1) accessory genes: requirement of a site in the nef gene for HIV-1 replication in activated $CD4^+$ T cells *in vitro* and *in vivo*. J Virol 71: 8456–8466.
34. Adachi A, Gendelman HE, Koenig S, Folks T, Willey R, et al. (1986) Production of acquired immunodeficiency syndrome-associated retrovirus in human and nonhuman cells transfected with an infectious molecular clone. J Virol 59: 284–291.
35. Goh WC, Rogel ME, Kinsey CM, Michael SF, Fultz PN, et al. (1998) HIV-1 Vpr increases viral expression by manipulation of the cell cycle: a mechanism for selection of Vpr *in vivo*. Nat Med 4: 65–71.
36. Vieillard V, Strominger JL, Debre P (2005) NK cytotoxicity against $CD4^+$ T cells during HIV-1 infection: a gp41 peptide induces the expression of an NKp44 ligand. Proc Natl Acad Sci U S A 102: 10981–10986.
37. Chang JJ, Altfeld M (2010) Innate immune activation in primary HIV-1 infection. J Infect Dis 202 Suppl 2: S297–301.
38. Ward J, Davis Z, DeHart J, Zimmerman E, Bosque A, et al. (2009) HIV-1 Vpr triggers natural killer cell-mediated lysis of infected cells through activation of the ATR-mediated DNA damage response. PLoS Pathog 5: e1000613.
39. Richard J, Sindhu S, Pham TN, Belzile JP, Cohen EA (2010) HIV-1 Vpr up-regulates expression of ligands for the activating NKG2D receptor and promotes NK cell-mediated killing. Blood 115: 1354–1363.
40. Stevenson M, Stanwick TL, Dempsey MP, Lamonica CA (1990) HIV-1 replication is controlled at the level of T cell activation and proviral integration. EMBO J 9: 1551–1560.
41. Zack JA, Arrigo SJ, Weitsman SR, Go AS, Haislip A, et al. (1990) HIV-1 entry into quiescent primary lymphocytes: molecular analysis reveals a labile, latent viral structure. Cell 61: 213–222.
42. Salazar-Gonzalez JF, Salazar MG, Keele BF, Learn GH, Giorgi EE, et al. (2009) Genetic identity, biological phenotype, and evolutionary pathways of transmitted/founder viruses in acute and early HIV-1 infection. J Exp Med 206: 1273–1289.
43. Jowett JB, Planelles V, Poon B, Shah NP, Chen ML, et al. (1995) The human immunodeficiency virus type 1 vpr gene arrests infected T cells in the G2+M phase of the cell cycle. J Virol 69: 6304–6313.
44. Rogel ME, Wu LI, Emerman M (1995) The human immunodeficiency virus type 1 *vpr* gene prevents cell proliferation during chronic infection. J Virol 69: 882–888.
45. Parrish NF, Wilen CB, Banks LB, Iyer SS, Pfaff JM, et al. (2012) Transmitted/founder and chronic subtype C HIV-1 use CD4 and CCR5 receptors with equal efficiency and are not inhibited by blocking the integrin $\alpha4\beta7$. PLoS Pathog 8: e1002686.
46. Keele BF, Giorgi EE, Salazar-Gonzalez JF, Decker JM, Pham KT, et al. (2008) Identification and characterization of transmitted and early founder virus envelopes in primary HIV-1 infection. Proc Natl Acad Sci U S A 105: 7552–7557.
47. Koot M, van 't Wout AB, Kootstra NA, de Goede RE, Tersmette M, et al. (1996) Relation between changes in cellular load, evolution of viral phenotype, and the clonal composition of virus populations in the course of human immunodeficiency virus type 1 infection. J Infect Dis 173: 349–354.
48. Mosier DE (2009) How HIV changes its tropism: evolution and adaptation? Curr Opin HIV AIDS 4: 125–130.
49. Brenchley JM, Silvestri G, Douek DC (2010) Nonprogressive and progressive primate immunodeficiency lentivirus infections. Immunity 32: 737–742.
50. Brenchley JM, Schacker TW, Ruff LE, Price DA, Taylor JH, et al. (2004) $CD4^+$ T cell depletion during all stages of HIV disease occurs predominantly in the gastrointestinal tract. J Exp Med 200: 749–759.
51. Veazey RS, DeMaria M, Chalifoux LV, Shvetz DE, Pauley DR, et al. (1998) Gastrointestinal tract as a major site of $CD4^+$ T cell depletion and viral replication in SIV infection. Science 280: 427–431.
52. Giavedoni LD, Velasquillo MC, Parodi LM, Hubbard GB, Hodara VL (2000) Cytokine expression, natural killer cell activation, and phenotypic changes in lymphoid cells from rhesus macaques during acute infection with pathogenic simian immunodeficiency virus. J Virol 74: 1648–1657.

53. Emilie D, Peuchmaur M, Maillot MC, Crevon MC, Brousse N, et al. (1990) Production of interleukins in human immunodeficiency virus-1-replicating lymph nodes. J Clin Invest 86: 148–159.
54. Brenchley JM, Price DA, Schacker TW, Asher TE, Silvestri G, et al. (2006) Microbial translocation is a cause of systemic immune activation in chronic HIV infection. Nat Med 12: 1365–1371.
55. Akira S, Takeda K, Kaisho T (2001) Toll-like receptors: critical proteins linking innate and acquired immunity. Nat Immunol 2: 675–680.
56. Sauter B, Albert ML, Francisco L, Larsson M, Somersan S, et al. (2000) Consequences of cell death: exposure to necrotic tumor cells, but not primary tissue cells or apoptotic cells, induces the maturation of immunostimulatory dendritic cells. J Exp Med 191: 423–434.
57. Basu S, Binder RJ, Suto R, Anderson KM, Srivastava PK (2000) Necrotic but not apoptotic cell death releases heat shock proteins, which deliver a partial maturation signal to dendritic cells and activate the NF-κB pathway. Int Immunol 12: 1539–1546.
58. Ostrand-Rosenberg S, Sinha P, Beury DW, Clements VK (2012) Cross-talk between myeloid-derived suppressor cells (MDSC), macrophages, and dendritic cells enhances tumor-induced immune suppression. Semin Cancer Biol 22: 275–281.
59. Gabrilovich DI, Nagaraj S (2009) Myeloid-derived suppressor cells as regulators of the immune system. Nat Rev Immunol 9: 162–174.
60. Gorantla S, Makarov E, Finke-Dwyer J, Gebhart CL, Domm W, et al. (2010) $CD8^+$ cell depletion accelerates HIV-1 immunopathology in humanized mice. J Immunol 184: 7082–7091.
61. Baenziger S, Tussiwand R, Schlaepfer E, Mazzucchelli L, Heikenwalder M, et al. (2006) Disseminated and sustained HIV infection in $CD34^+$ cord blood cell-transplanted $Rag2^{-/-}\gamma_c^{-/-}$ mice. Proc Natl Acad Sci U S A 103: 15951–15956.
62. Watanabe S, Ohta S, Yajima M, Terashima K, Ito M, et al. (2007) Humanized NOD/SCID/IL2Rγ^{null} mice transplanted with hematopoietic stem cells under nonmyeloablative conditions show prolonged life spans and allow detailed analysis of human immunodeficiency virus type 1 pathogenesis. J Virol 81: 13259–13264.
63. Watanabe S, Terashima K, Ohta S, Horibata S, Yajima M, et al. (2007) Hematopoietic stem cell-engrafted NOD/SCID/IL2Rγ^{null} mice develop human lymphoid systems and induce long-lasting HIV-1 infection with specific humoral immune responses. Blood 109: 212–218.
64. Sato K, Koyanagi Y (2011) The mouse is out of the bag: insights and perspectives on HIV-1-infected humanized mouse models. Exp Biol Med (Maywood) 236: 977–985.
65. Berges BK, Rowan MR (2011) The utility of the new generation of humanized mice to study HIV-1 infection: transmission, prevention, pathogenesis, and treatment. Retrovirology 8: 65.
66. Shultz LD, Brehm MA, Garcia-Martinez JV, Greiner DL (2012) Humanized mice for immune system investigation: progress, promise and challenges. Nat Rev Immunol 12: 786–798.
67. Levy DN, Refaeli Y, MacGregor RR, Weiner DB (1994) Serum Vpr regulates productive infection and latency of human immunodeficiency virus type 1. Proc Natl Acad Sci U S A 91: 10873–10877.
68. Hoshino S, Sun B, Konishi M, Shimura M, Segawa T, et al. (2007) Vpr in plasma of HIV type 1-positive patients is correlated with the HIV type 1 RNA titers. AIDS Res Hum Retroviruses 23: 391–397.
69. Zimmerman ES, Sherman MP, Blackett JL, Neidleman JA, Kreis C, et al. (2006) Human immunodeficiency virus type 1 Vpr induces DNA replication stress *in vitro* and *in vivo*. J Virol 80: 10407–10418.
70. Sakai K, Dimas J, Lenardo MJ (2006) The Vif and Vpr accessory proteins independently cause HIV-1-induced T cell cytopathicity and cell cycle arrest. Proc Natl Acad Sci U S A 103: 3369–3374.
71. Wang J, Shackelford JM, Casella CR, Shivers DK, Rapaport EL, et al. (2007) The Vif accessory protein alters the cell cycle of human immunodeficiency virus type 1 infected cells. Virology 359: 243–252.
72. Izumi T, Io K, Matsui M, Shirakawa K, Shinohara M, et al. (2010) HIV-1 viral infectivity factor interacts with TP53 to induce G2 cell cycle arrest and positively regulate viral replication. Proc Natl Acad Sci U S A 107: 20798–20803.
73. Ito M, Hiramatsu H, Kobayashi K, Suzue K, Kawahata M, et al. (2002) NOD/SCID/γ_c^{null} mouse: an excellent recipient mouse model for engraftment of human cells. Blood 100: 3175–3182.
74. An DS, Poon B, Ho Tsong Fang R, Weijer K, Blom B, et al. (2007) Use of a novel chimeric mouse model with a functionally active human immune system to study human immunodeficiency virus type 1 infection. Clin Vaccine Immunol 14: 391–396.

Published August 26, 2013, doi:10.4049/jimmunol.1203543

Establishment of a Human Allergy Model Using Human IL-3/GM-CSF–Transgenic NOG Mice

Ryoji Ito,*,† Takeshi Takahashi,* Ikumi Katano,* Kenji Kawai,* Tsutomu Kamisako,* Tomoyuki Ogura,* Miyuki Ida-Tanaka,* Hiroshi Suemizu,* Satoshi Nunomura,‡ Chisei Ra,‡ Akio Mori,§ Sadakazu Aiso,† and Mamoru Ito*

The development of animal models that mimic human allergic responses is crucial to study the pathophysiology of disease and to generate new therapeutic methodologies. Humanized mice reconstituted with human immune systems are essential to study human immune reactions in vivo and are expected to be useful for studying human allergies. However, application of this technology to the study of human allergies has been limited, largely because of the poor development of human myeloid cells, especially granulocytes and mast cells, which are responsible for mediating allergic diseases, in conventional humanized mice. In this study, we developed a novel transgenic (Tg) strain, NOD/Shi-*scid*-IL2rγ^{null} (NOG), bearing human *IL-3* and *GM-CSF* genes (NOG IL-3/GM–Tg). In this strain, a large number of human myeloid cells of various lineages developed after transplantation of human CD34$^+$ hematopoietic stem cells. Notably, mature basophils and mast cells expressing FcεRI were markedly increased. These humanized NOG IL-3/GM–Tg mice developed passive cutaneous anaphylaxis reactions when administered anti–4-hydroxy-3-nitrophenylacetyl IgE Abs and 4-hydroxy-3-nitrophenylacetyl. More importantly, a combination of serum from Japanese cedar pollinosis patients and cedar pollen extract also elicited strong passive cutaneous anaphylaxis responses in mice. Thus, to our knowledge, our NOG IL-3/GM–Tg mice are the first humanized mouse model to enable the study of human allergic responses in vivo and are excellent tools for preclinical studies of allergic diseases. *The Journal of Immunology*, **2013, 191: 000–000.**

Rodent models for human allergies, including atopic dermatitis (1), asthma (2), allergic rhinitis (3), and food allergies (4, 5), have allowed researchers to elucidate important fundamental principles of the cellular and molecular mechanisms of these diseases. However, it was suggested that animal models do not always reflect all aspects of human allergic diseases because of differences between species. The gap between these animal models and human clinical settings has prevented the development of effective therapeutic strategies for the treatment of human allergies.

Reconstitution of human hematopoietic and immune systems in immunodeficient mouse strains was a major advance in the field of humanized mouse technologies within the last 2 decades. These mouse models were expected to recapitulate various human diseases, including cancer (6–9), infectious disease (10–14), and graft-versus-host-disease (GVHD) (15, 16), and to enhance basic research in human physiology and pathology, as well as the development of clinical drugs. Recently, severely immunodeficient mouse strains, such as NOD/Shi-*scid* IL2rγ^{null} (NOG) (17–19), NOD/LtSz-*scid* IL2rγ^{null} (NSG) (20), and BALB/c Rag2^{null} IL2rγ^{null} (21, 22), enabled long-term engraftment of human tissues because of the total lack of the endogenous mouse immune system, enormously improving the generation of humanized mice. Our group previously demonstrated that efficient human hematopoiesis could be seen in NOG mice upon transplantation of human hematopoietic stem cells (HSCs; hu-HSC NOG mice) (17, 23). In particular, lymphopoiesis was evident, and human B and T cells accounted for the majority of human cells in hu-HSC NOG mice. Accumulating evidence suggests that these human lymphocytes can mediate proper immune reactions, even if the response remains suboptimal. In contrast, the differentiation of human myeloid lineage cells, especially granulocytes and mast cells, in conventional hu-HSC NOG mice has been inefficient (23, 24). Considering the emerging roles of granulocytes and mast cells in allergic inflammatory diseases, it is important to establish useful animal models in which we can analyze and manipulate the functions of human granulocytes and mast cells. Poor differentiation of these cells may be attributed, in part, to an insufficient supply of cytokines, such as G-CSF, GM-CSF, IL-3, IL-6, Fms-related tyrosine kinase 3 ligand, thrombopoietin (TPO), and stem cell factor (SCF) (25–29). Recently, several groups attempted to improve the efficiency of human granulopoiesis in humanized mice by engineering mice to express human genes encoding these cytokines. Billerbeck et al. (30) developed a transgenic (Tg) NSG mouse strain expressing human (h) SCF, hGM-CSF, and hIL-3 (SGM3-Tg) and demonstrated that the development of CD33$^+$ myeloid cells and CD15$^+$ granulocytes was

*Central Institute for Experimental Animals, Kawasaki-ku, Kawasaki, Kanagawa 210-0821, Japan; †Department of Anatomy, Keio University School of Medicine, Shinjuku-ku, Tokyo 160-8582, Japan; ‡Division of Molecular Cell Immunology and Allergology, Nihon University, Graduate School of Medical Science, Itabashi-ku, Tokyo 173-8610, Japan; and §National Hospital Organization, Sagamihara National Hospital, Clinical Research Center, Minami-ku, Sagamihara, Kanagawa 252-0315, Japan

Received for publication December 27, 2012. Accepted for publication July 16, 2013.

This work was supported by a grant from the Research Foundation for Pharmaceutical Sciences and by Grants-in-Aid for Young Scientists (B) 22700458 and Scientific Research (S) 22220007 from the Ministry of Education, Culture, Sports, Science and Technology of Japan.

Address correspondence and reprint requests to Dr. Mamoru Ito, Central Institute for Experimental Animals, 3-25-12 Tonomachi, Kawasaki-ku, Kawasaki, Kanagawa 210-0821, Japan. E-mail address: mito@ciea.or.jp

The online version of this article contains supplemental material.

Abbreviations used in this article: BALF, bronchoalveolar lavage fluid; BM, bone marrow; CIEA, Central Institute for Experimental Animals; GVHD, graft-versus-host disease; h, human; HSC, hematopoietic stem cell; KI, knock-in; m, mouse; MCC, mast cell chymase; MCT, mast cell containing tryptase; MCTC, mast cell containing tryptase and chymase; NOG, NOD/Shi-*scid* IL2rγ^{null}; NP, 4-hydroxy-3-nitrophenylacetyl; NSG, NOD/LtSz-*scid* IL2rγ^{null}; PB, peripheral blood; PCA, passive cutaneous anaphylaxis; SCF, stem cell factor; Tg, transgenic; TPO, thrombopoietin.

www.jimmunol.org/cgi/doi/10.4049/jimmunol.1203543

slightly enhanced in SGM3-Tg mice compared with non-Tg control mice following transplantation with hHSCs. Furthermore, Rongvaux et al. (31) established hTPO knock-in (KI) mice in which the mouse *TPO* gene locus was replaced with the corresponding human gene locus. Upon transplantation of hHSCs, this strain showed remarkable differentiation of monocytes and granulocytes. However, generation of mast cells and several granulocyte subpopulations remained insufficient. Moreover, although the efficient development of human granulocytes and mast cells was demonstrated in humanized membrane-bound SCF-Tg NSG mice (32), the function of granulocytes in humanized SCF-Tg NSG mice has not been verified, especially with respect to whether they could release cytoplasmic granules containing histamine, leukotriene, and so forth in response to stimulation.

In this study, we generated a novel NOG substrain: hIL-3 and hGM-CSF–Tg (IL-3/GM–Tg) NOG mice. Within this model, we studied the development of human myeloid cells, maturation of basophils and mast cells, and passive cutaneous anaphylaxis (PCA) reaction in response to Ag-specific hIgE and the specific Ags. Our results effectively support the usefulness of this novel platform for studying human allergies.

Materials and Methods

Ethics statement

All animal experiments were approved by the Institutional Animal Care and Use Committee of the Central Institute for Experimental Animals (CIEA) and were performed in accordance with guidelines set forth by the CIEA.

All experiments using human cells and serum were approved by the institutional ethical committee of the CIEA and Sagamihara National Hospital. Written informed consent was obtained from every subject enrolled in the current study.

Generation of NOG IL-3/GM–Tg mice

Previously, we established a hIL-3 and hGM-CSF Tg C57BL/6J-*scid* mouse strain in which the Tg human genes were ubiquitously expressed under control of the SRα promoter (33). This strain was backcrossed six times with NOG (formal name: NOD.Cg-*prkdc*^{scid}*il2r*γ^{tm1Sug}/ShiJic) mice to replace the genetic background with the aid of a marker-assisted selection protocol. Serum levels of hIL-3 and hGM-CSF were measured using human IL-3 and human GM-CSF Quantikine ELISA Kits (R&D Systems, Minneapolis, MN). The mice were maintained in the CIEA under specific pathogen–free conditions.

Human HSC transplantation

Human umbilical cord blood–derived CD34$^+$ cells were purchased from Lonza (cat. no. 2C-101A; Basel, Switzerland). After thawing the frozen vials of cells according to the manufacturer's protocol, cells with >90% viability were used for transplantation. NOG IL-3/GM–Tg or non-Tg mice (8–10 wk old) were irradiated with x-rays (2.5 Gy; MBR-1505R; Hitachi Medical, Tokyo, Japan). After 24 h, 4–5 × 10^4 hHSCs were transplanted i.v. via the tail vein.

Flow cytometry

Bone marrow (BM), spleen, peripheral blood (PB), and bronchoalveolar lavage fluid (BALF) tissues were obtained from mice transplanted with hHSCs. Single mononuclear cell suspensions were prepared by standard methods, and RBCs were eliminated using BD Pharm Lyse (BD Biosciences, San Jose, CA). Human PB samples were obtained from healthy volunteers after acquiring their informed consent. hPBMCs were isolated by Ficoll-Hypaque (GE Healthcare, Little Chalfont, Buckinghamshire, U.K.) density centrifugation and washed with PBS. The cells were incubated with appropriate fluorochrome-conjugated Abs for 15–20 min at 4°C. After washing with FACS buffer containing PBS with 1% FCS, the cells were resuspended in propidium iodide solution (BD Biosciences). Fluorescent signals were measured using a FACSCanto multicolor flow cytometer, and the data were analyzed using FACSDiva software (both from BD Biosciences). We used the following Abs: anti-hCD33–FITC and anti–mouse (m)CD45–biotin (BD Biosciences); anti-hCD19–PE (Beckman Coulter, Brea, CA); and anti-hCD45–allophycocyanin–Cy7, anti-hCD66b–FITC, anti-hLineage mixture (CD3, CD14, CD19, CD20, CD56)–FITC, anti-hCD56–PE, anti-hCD203c–PE, anti-hCD38–PE, anti-hCD34–PE–Cy7, anti-hCD3–PE–Cy7, anti–hc-kit–PE–Cy7, anti-CD14–PE–Cy7, anti-hFcεRI–allophycocyanin, and anti-hCD11c–allophycocyanin (BioLegend, San Diego, CA).

Determination of human granulocytes

At 11 wk after HSC transplantation, PB was collected from the orbital vein of humanized NOG IL-3/GM–Tg and non-Tg NOG mice under anesthesia. Single-cell suspensions were prepared using BD Pharm Lyse (BD Biosciences), and hCD45$^+$ cells were purified by eliminating mCD45$^+$ cells using MACS. Briefly, the cells were stained with biotinylated anti-mCD45 Abs in MACS running buffer (PBS containing 2 mM EDTA and 0.1% BSA) for 15 min at 4°C. The cells were washed with MACS buffer and subsequently labeled with anti-biotin magnetic beads (Miltenyi Biotec, Sunnyvale, CA). Labeled mCD45$^+$ cells were eliminated using a MACS LS column (Miltenyi Biotec). The purity of hCD45$^+$ cells in the negative fraction was typically 95–99%.

For May–Grünwald–Giemsa staining, enriched hCD45$^+$ cells were smeared onto glass slides and air dried for 10 min. The slides were soaked in May–Grünwald solution (Muto Pure Chemicals, Tokyo, Japan) for 3 min and then washed with running water to remove excess stain. The slides were further stained with 0.5% Giemsa solution (Muto Pure Chemicals) for 15 min. After washing with running water, the slides were dried and subjected to microscopic analyses.

In vitro stimulation of human basophils and mast cells

At 18 wk after HSC transplantation, BM mononuclear cells from NOG IL-3/GM–Tg mice and hPBMCs were stimulated with 1 μg/ml ionomycin (Sigma-Aldrich, St. Louis, MO) for 30 min at 37°C in a 5% CO_2 incubator. After stimulation, these cells were stained with allophycocyanin-Cy7–anti-hCD45, FITC–anti-hCD63 (Beckman Coulter), PE–anti-hCD203, and allophycocyanin–anti-hFcεR mAbs and were analyzed by flow cytometer.

Immunohistochemistry

For histological analyses, the lungs, spleen, stomach, and skin from humanized NOG IL-3/GM–Tg and non-Tg mice were fixed with 4% paraformaldehyde (Wako, Osaka, Japan) and embedded in paraffin. The samples were then serially sectioned to a thickness of 3 μm using a microtome and placed on silane-coated slides (Muto Pure Chemicals). After deparaffinization, sections were incubated overnight at 4°C with anti-human mast cell chymase (MCC) Abs (clone CC1; Leica Microsystems, Tokyo, Japan) and anti-human FcεRI Ab (clone CRA-1) (34, 35) and then incubated with a peroxidase-labeled polymer-conjugated anti-mouse Ab (Histofine Simple Stain Max-PO; Nichirei Biosciences, Tokyo, Japan) for 30 min at room temperature. For color development, the sections were incubated with a 0.02% solution of the substrate 3,3′-diaminobenzidine (Dojindo, Kumamoto, Japan) containing 0.006% H_2O_2. Immunostained sections were counterstained with hematoxylin (Sakura Finetech, Tokyo, Japan) for visualization of nuclei. For immunofluorescence staining, 4-μm-thick frozen sections of tissues were fixed in 99% ethanol for 30 min and incubated with 10% normal goat serum (Nichirei Biosciences) for 30 min. An anti-human mast cell tryptase mAb (clone 10D11; Leica Microsystems) or an anti-human MCC mAb was fluorescently labeled with either Alexa Fluor 488 or Alexa Fluor 546 using a Zenon Mouse IgG2b or IgG1 Kit (Life Technologies, Carlsbad CA), according to the manufacturer's instructions, and we used these mAbs for double staining of the sections. After a 2-h incubation at room temperature, the sections were washed five times with PBS and mounted with ImmunoSelect Antifading Mounting Medium DAPI (Dianova, Hamburg, Germany). The specimens were visualized by fluorescence microscopy (Axio Imager M1; Carl Zeiss Microscopy, Tokyo Japan).

PCA reactions

An anti–4-hydroxy-3-nitrophenylacetyl (NP) human/mouse chimeric IgE Ab (Serotec, Oxford, U.K.), which is composed of murine V region and human C region, was injected intradermally at six locations (0.5 μg/location) on the dorsal side of humanized NOG IL-3/GM–Tg, non-Tg, and nonhumanized NOG mice. The same amount of hIgE Ab (Abcam, Tokyo, Japan) was injected into the ventral side of the mice as negative controls. Twenty-four hours after sensitization, the mice were injected i.v. with 500 μg NP-conjugated BSA (Biosearch Technologies, Novato, CA) with 0.5% Evans blue dye. Extravasation of the dye was visualized 30 min later by observing the blue staining of the reverse-side sites on the opposite side of the injection sites. For pollinosis PCA reaction, Japanese cedar pollinosis patients were recruited from the outpatient clinic of Sagamihara National Hospital. Japanese cedar pollen–specific IgE titer in the serum was determined by CAP-RAST. Serum obtained from Japanese cedar

Table I. Generation of hIL-3/GM-CSF–Tg NOG mice

Generation	NOD Marker (%)	Cytokine Levels in Sera (pg/ml) hIL−3	hGM−CSF
N0	0	ND	ND
N1	50	ND	ND
N2	81	ND	ND
N3	93	106.7 ± 14.7	67.1 ± 27.5
N4	98	ND	ND
N5	98	74.4 ± 44.7	51.4 ± 40.5
N6	100	ND	ND
N7	100	82.04 ± 40.24	35.03 ± 11.6

ND, Not determined.

pollinosis patients (carrier polymer radioallergosorbent score = 5) was diluted 2-fold in saline and injected intradermally at two locations on the dorsal side of the mice. After 24 h, these mice were injected i.v. with 100 μl the cedar pollen extract (200 JAU/ml; Torii Pharmaceutical, Tokyo, Japan) with 0.5% Evans blue dye. After 30 min, dorsal or ventral skins from these mice were isolated and weighed. Evans blue dye was extracted from the skin by incubation in 5 ml formamide at 60°C overnight and quantified by OD at 620 nm in a spectrometer (Bio-Rad, Tokyo, Japan).

Statistical analysis

Mean values and SD were calculated using Microsoft Excel (Microsoft, Redmond, WA). Student *t* tests were used to identify significant differences.

Results

Generation of NOG IL-3/GM–Tg mice

We generated NOG IL-3/GM–Tg mice by speed congenic techniques using a marker-assisted selection protocol (36) to change the genetic background of the mice from C57BL/6J to NOD. IL-3/GM–Tg mice, in which all of the microsatellite markers were replaced by the NOD haplotype at N6, were further crossed onto the NOG background. We confirmed the expression of the hIL-3 and hGM-CSF transgenes in the N3, N5, and N7 generations (Table I). For hHSC transfer, we used NOG IL-3/GM–Tg mice backcrossed more than seven times.

Human hematopoiesis in hu-HSC NOG IL-3/GM–Tg mice

To investigate the effects of hIL-3 and hGM-CSF on hematopoiesis in humanized mice, we transplanted hCD34$^+$ HSCs into NOG IL-3/GM–Tg and non-Tg mice. The frequencies of hCD45$^+$ cells and various lineages of human leukocytes in PB and various tissues

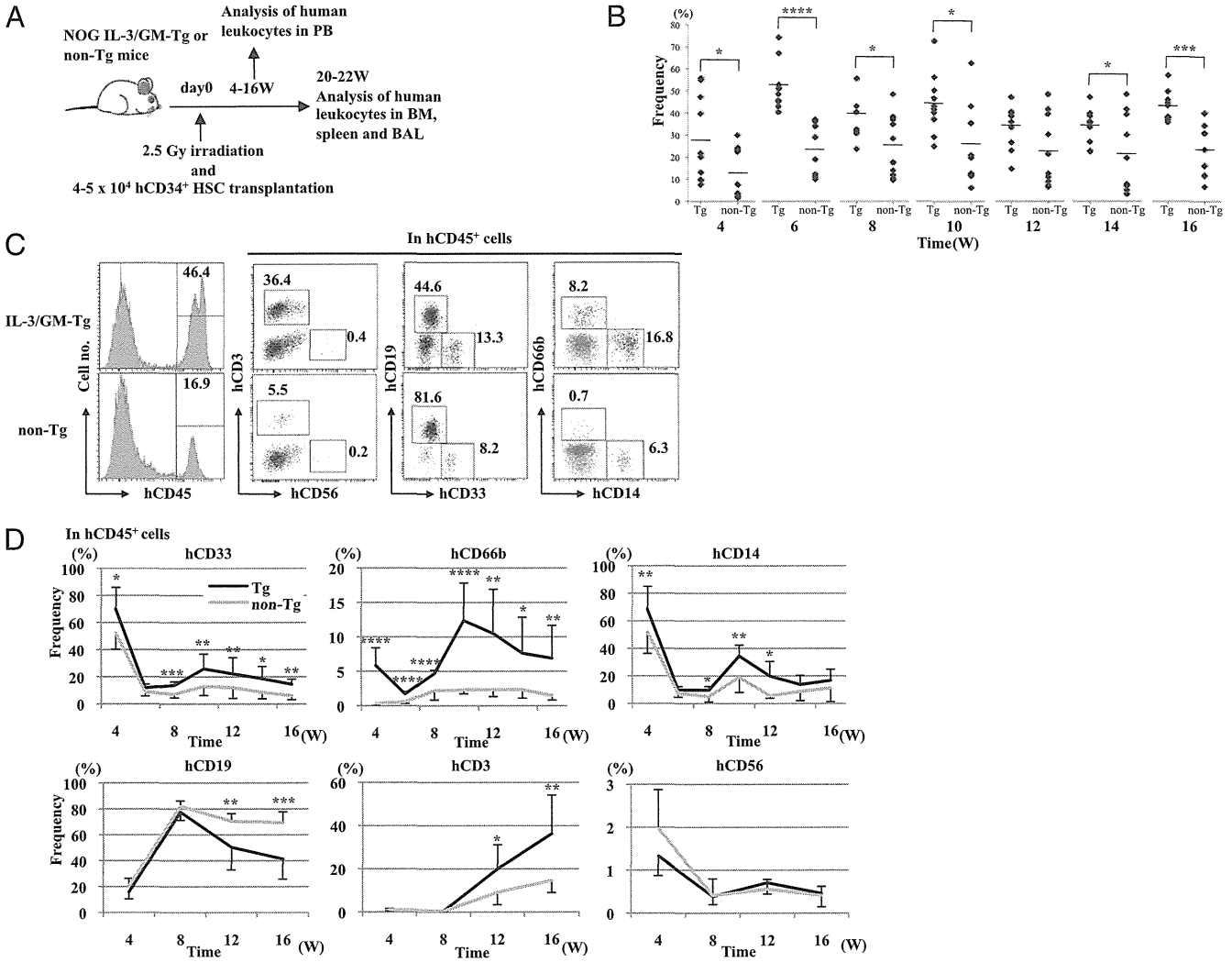

FIGURE 1. Human hematopoiesis in NOG IL-3/GM–Tg mice. (**A**) Schematic view of the reconstitution of human immune systems in NOG IL-3/GM–Tg mice. NOG IL-3/GM–Tg mice and non-Tg littermates (8–10 wk old) were transplanted with 4–5 × 10^4 hCD34$^+$ HSCs 1 d after x-ray irradiation (2.5 Gy). Human leukocytes were analyzed at the indicated time points. (**B**) Kinetics of hCD45$^+$ cell engraftment. The frequency of human leukocytes in PB was analyzed by flow cytometry at the indicated time points over 12 wk. Data are mean ± SD (n = 10 mice/group). (**C** and **D**) Frequencies of engrafted multilineage hCD19$^+$, hCD3$^+$, hCD56$^+$, hCD33$^+$, hCD66b$^+$, and hCD14$^+$ human leukocytes in the hCD45$^+$ cell population were analyzed by flow cytometry. *$p < 0.05$, **$p < 0.005$, ***$p < 0.0005$, ****$p < 0.00005$.

from these mice were analyzed at different time points (Fig. 1A). The chimerism of hCD45$^+$ cells in PB was significantly higher in hu-HSC NOG IL-3/GM–Tg mice than in non-Tg NOG mice throughout the analysis period (Fig. 1B, 1C). For the myeloid lineage, hu-HSC NOG IL-3/GM–Tg mice had significantly higher frequencies of total hCD33$^+$ myeloid cells, hCD66b$^+$ granulocytes, and hCD14$^+$ monocytes than did non-Tg mice (Fig. 1C, 1D). In particular, the increase in hCD66b$^+$ granulocytes was dramatic compared with the low differentiation of this population in conventional NOG mice. For lymphoid cells, the increase in the hCD3$^+$ T cell population was more evident in Tg mice than in non-Tg mice at 12 wk post-HSC transplantation, resulting in a lower frequency of hCD19$^+$ B cells in Tg mice than in non-Tg mice; the development of hCD56$^+$ NK cells was not influenced (Fig. 1C, 1D). Human leukocytes, other than lymphoid and myeloid lineage cells, were scarce in hCD45$^+$ cells in PB of Tg and non-Tg mice (Supplemental Fig. 1A).

We next investigated other organs. The engraftment of human HSCs, defined as hCD34$^+$hCD38$^-$ cells in hCD45$^+$lineage$^-$ cells, in the BM showed 4- and 3-fold increases in frequency and cell number, respectively, in Tg mice compared with non-Tg mice (Fig. 2A, 2B). Spleens were markedly enlarged in hu-HSC NOG IL-3/GM–Tg mice (Supplemental Fig. 1B). Consistent with this finding, weight and total splenocyte numbers were ~3-fold higher in Tg mice than in non-Tg mice (Supplemental Fig. 1C, 1D). Although the percentage of CD45$^+$ cells did not differ between Tg and non-Tg mice, the absolute number of hCD45$^+$ cells increased in Tg mice, reflecting an increase in total cell number (Fig. 2C, 2D). As in the PB, the frequency and absolute number of hCD33$^+$ myeloid cells in the spleen were increased in hu-HSC–Tg mice, and expansion of hCD66b$^+$ granulocytes was especially remarkable (Fig. 2D, 2E). An increase in the hCD33$^+$hCD11c$^+$ myeloid dendritic cell population was also confirmed (Fig. 2D, 2E). In addition, the number of cells in BALF samples was increased 4-

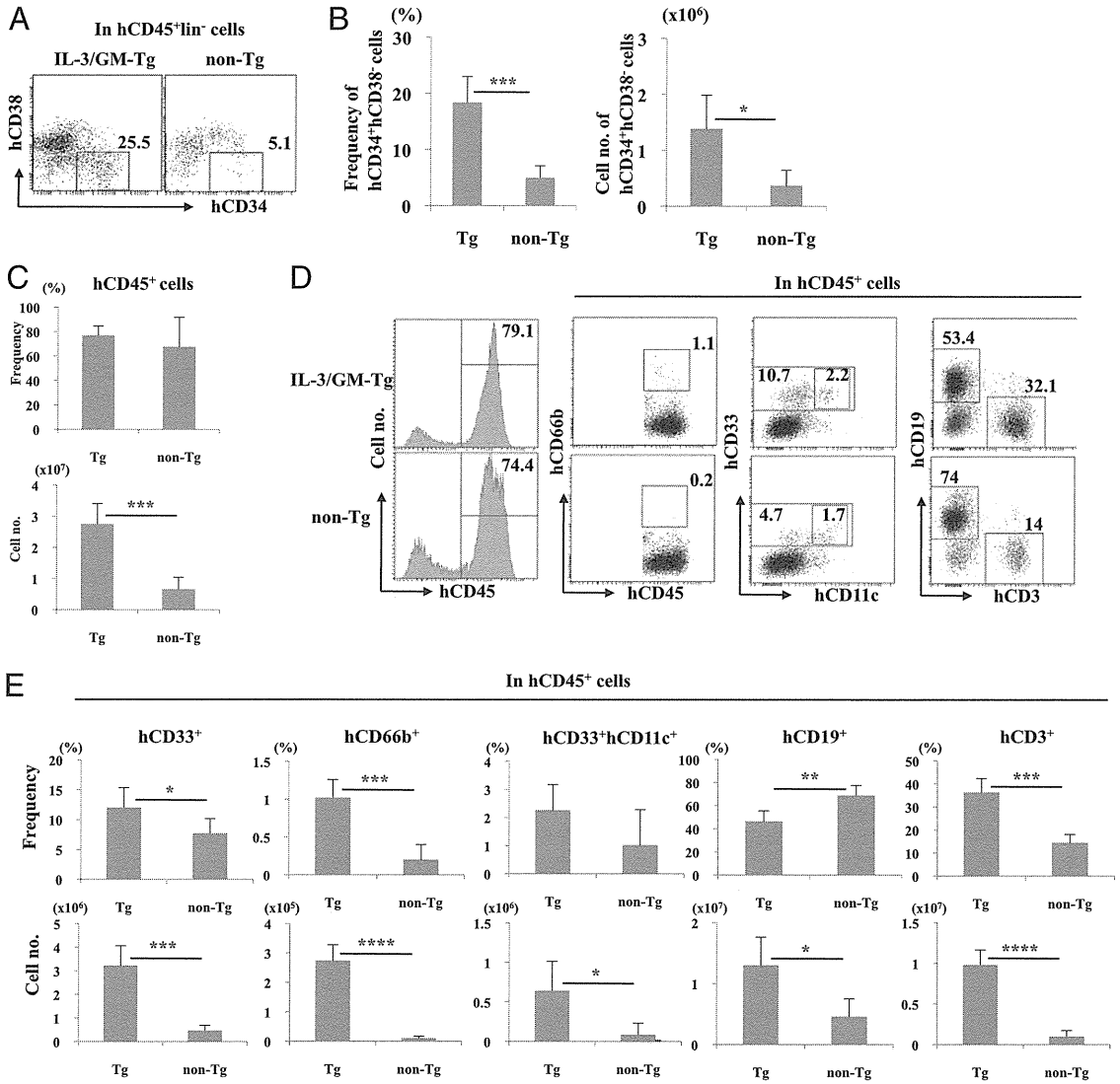

FIGURE 2. Analysis of the BM and spleen in NOG IL-3/GM–Tg mice. BM cells were isolated from the tibiae of hu-HSC NOG IL-3/GM–Tg and non-Tg mice and stained with anti-hCD34, anti-hCD38, and anti-hCD45 Abs and anti-lineage markers to identify hHSCs (hCD34$^+$hCD38$^-$ cells in the hCD45$^+$ lineage$^-$). A representative HSC staining pattern (**A**) and the mean frequency and cell numbers [(**B**), n = 5/group] are shown. (**C**–**E**) After the preparation of splenocytes from hu-HSC NOG–Tg and non-Tg mice at 20–22 wk postreconstitution, the total number of cells was counted, and the cells were stained with various Abs to facilitate analysis by flow cytometry. (C) Frequency (*upper panel*) and number (*lower panel*) of hCD45$^+$ human leukocytes. Data are the mean ± SD (n = 5 mice/group). (D and E) Differentiation of human myeloid and lymphoid cells in hu-HSC NOG IL-3/GM–Tg mice. After staining with Abs specific for myeloid (hCD33, hCD66b, and hCD11c) and lymphoid (hCD19 and hCD3) markers, the cells were analyzed by flow cytometry. (**D**) Representative plots. (**E**) Frequency (*upper panels*) and absolute cell number (*lower panels*) for each hCD45$^+$ cell subpopulation. Absolute cell number was calculated by multiplying the frequency by the total cell number. *$p < 0.05$, **$p < 0.005$, ***$p < 0.0005$, ****$p < 0.00005$.

fold in hu-HSC NOG IL-3/GM–Tg mice (Supplemental Fig. 1D), whereas there was no significant difference in BM cell numbers (Supplemental Fig. 1D). Overall, the numbers of myeloid cells were increased in BM and BALF samples from hu-HSC NOG IL-3/GM–Tg mice (Supplemental Fig. 1E, 1F). For lymphoid lineage cells, the T cell population was significantly larger in all tissues from hu-HSC NOG IL-3/GM–Tg mice compared with non-Tg mice in terms of both frequency and absolute cell number (Fig. 2E, Supplemental Fig. 1E, 1F). The frequency of B cells was lower in spleen and BM from hu-HSC NOG IL-3/GM–Tg mice than in non-Tg mice (Fig. 2E, Supplemental Fig. 1E). Nevertheless, the number of B cells was higher in spleen and BALF tissues from hu-HSC NOG IL-3/GM–Tg mice compared with non-Tg mice (Fig. 2E, Supplemental Fig. 1F). The increase in the total number of $hCD45^+$ cells may compensate for the reduction in the number of B cells in Tg mice. Following the marked improvement of the development of human myeloid cells, we also confirmed development of a large number of human macrophages in various tissues, including the liver, lung, and spleen, in hu-HSC NOG IL-3/GM–Tg mice (Supplemental Fig. 1G).

Taken together, these data demonstrate that human myelopoiesis, especially the development of granulocytes, was dramatically improved in NOG IL-3/GM–Tg mice.

Development of human granulocytes in hu-HSC NOG IL-3/GM–Tg mice

One of the main characteristics of HSC-transplanted NOG IL-3/GM–Tg mice was the efficient development of human granulocytes. Therefore, we examined whether these cells contain typical subpopulations (i.e., basophils, eosinophils, and neutrophils). To analyze the morphology of human granulocytes from hu-HSC NOG IL-3/GM–Tg and non-Tg mice, human leukocytes were purified from the PB by eliminating $mCD45^+$ cells. In the $hCD45^+$ cells from Tg mice, there was an $SSC^{midhi}hCD66b^+$ cell population, whereas no corresponding cell population existed in non-Tg mice (Fig. 3A). Smears of $hCD45^+$ cells from hu-HSC IL-3/GM–Tg mice, but not non-Tg mice, showed large numbers of leukocytes with intracellular granules and lobulated nuclei (Fig. 3B). At a higher magnification, we identified the cells containing red (Fig. 3C, *left panel*) or dark blue (Fig. 3C, *middle panel*) granules, which represented eosinophils and basophils, respectively. Although there also were cells whose nuclei had two lobules and small granules (Fig. 3C, *right panel*), these cells were presumably immature neutrophils. We detected no mature neutrophils with highly lobulated nuclei.

Development of mature basophils and mast cells in hu-HSC NOG IL-3/GM–Tg mice

Considering the pathogenic roles of basophils and mast cells in allergic responses, we were interested in determining whether these populations can be induced to enter a mature state in hu-HSC NOG IL-3/GM–Tg mice.

We examined whether human cells expressing FcεRI or CD203c, functional and phenotypic markers, respectively, were present. As shown in Fig. 4A, there was a clear subpopulation of $hFc\varepsilon RI^+$ $hCD203c^+$ cells, which represented basophils and mast cells, in PB, BM, spleen, and BALF samples from hu-HSC NOG IL-3/GM–Tg mice but not non-Tg mice. The frequencies and numbers of $hFc\varepsilon RI^+hCD203c^+$ cells were significantly higher in hu-HSC NOG IL-3/GM–Tg mice than in non-Tg mice (Fig. 4B). These data suggest that IL-3 and/or GM-CSF support the development of FcεR-expressing mature basophils and mast cells. We further distinguished mast cells and basophils by assessing hc-kit expression. As shown in Fig. 4C, all $hFc\varepsilon RI^+hCD203c^+$ cells were hc-kit^- (basophils) in human PBMCs. In contrast, ~20% of $hFc\varepsilon RI^+$ $hCD203c^+$ cells in the PB collected from hu-HSC IL-3/GM–Tg mice were hc-kit^+ (mast cells; Fig. 4C). When we compared the frequencies of basophils and mast cells in various tissues, ~70 and 50% of $hFc\varepsilon RI^+hCD203c^+$ cells in the spleen and BM, respectively, were mast cells (Fig. 4D), suggesting that these cell types were differentially distributed in various tissues. When we stimulated these $hFc\varepsilon RI^+hCD203c^+$ mast cells or basophils in BM of IL-3/GM–Tg mice, they showed elevated expression of CD63. The levels of CD63 were as high as those of basophils in human PBMCs, representing a marker of basophil and mast cell activation (37), which suggests that these cells were functional (Fig. 4E).

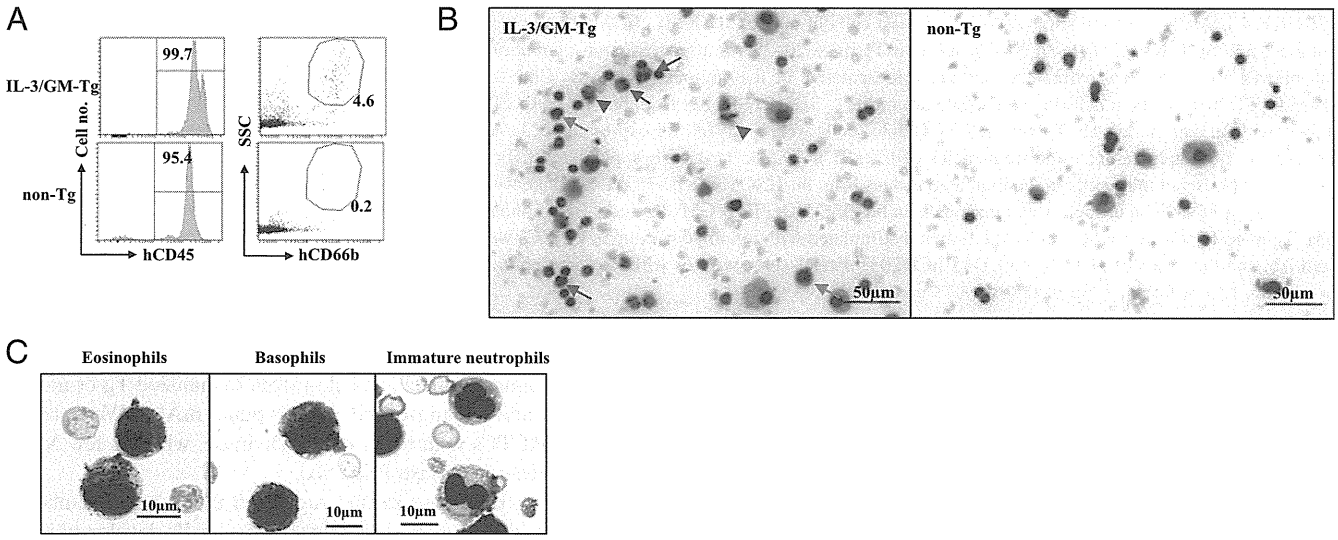

FIGURE 3. Development of human granulocytes in hu-HSC NOG IL-3/GM–Tg mice. (**A**) Human leukocytes were negatively enriched by >95% in the PB from hu-HSC NOG IL-3/GM–Tg or non-Tg mice at 11 wk after HSC transplantation. The $SSC^{midhi}CD66b^+$ fraction contained human granulocytes. (**B** and **C**) Smears of purified human leukocytes from hu-HSC NOG IL-3/GM–Tg and non-Tg mice were subjected to May–Giemsa staining. Red arrows identify eosinophils, which contained large red granules. Green arrows identify basophils, which contained small dark blue granules. Immature neutrophils were identified by small red granules (red arrowheads). (C) High magnification images of eosinophils, which contained large red granules (*left panel*); basophils, which contained small dark blue granules (*middle panel*) and immature neutrophils, which appear as small red granules (*right panel*). The data shown are representative of two independent experiments.

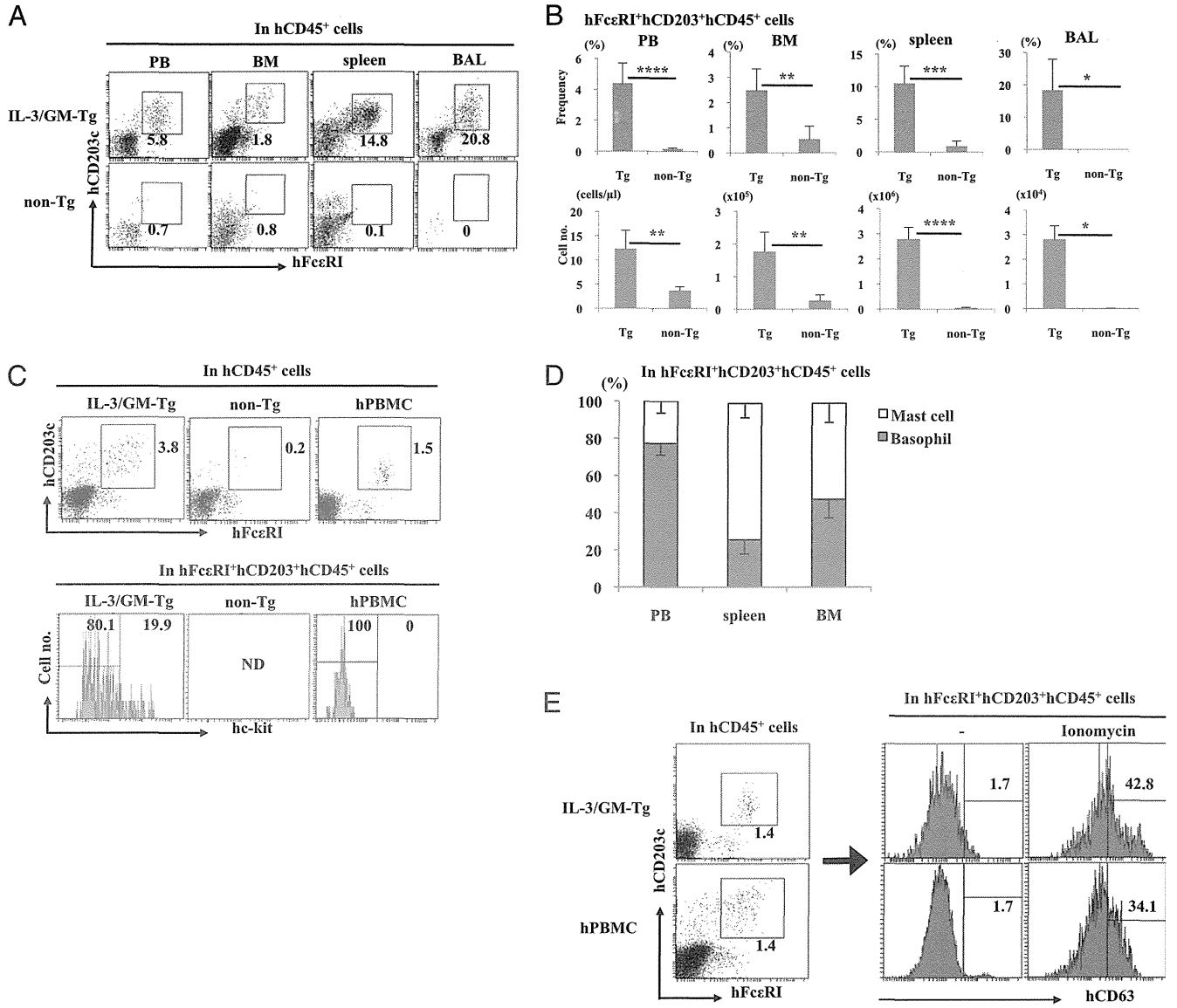

FIGURE 4. Analysis of human basophils and mast cells in hu-HSC NOG IL-3/GM–Tg mice. (**A**) Cells were isolated from PB, BM, spleen, and BALF samples from hu-HSC NOG IL-3/GM–Tg and non-Tg mice 20–22 wk after HSC transplantation and were stained with anti-hCD45, anti-hCD203c, and anti-hFcεRI Abs. The flow cytometry data are representative of five animals/group. (**B**) Cumulative data from (A). Frequency and absolute number of hFcεRI$^+$hCD203c$^+$ cells in hCD45$^+$ cells. Data are mean ± SD. (**C**) PBMCs from hu-HSC NOG IL-3/GM–Tg and non-Tg mice and hPBMCs were further stained with an anti–hc-kit Ab. The hFcεRI$^+$hCD203c$^+$ cells were analyzed for expression of hc-kit, and the data are shown as graphs (*lower panels*). The numbers in the graphs indicate the frequencies of hFcεRI$^+$hCD203c$^+$hc-kit$^-$ basophils and hFcεRI$^+$hCD203c$^+$hc-kit$^+$ mast cells. (**D**) The frequencies of human basophils and mast cells in the indicated tissues from hu-HSC NOG IL-3/GM–Tg mice were obtained as described in (C). Data are mean ± SD. (**E**) Expression of hCD63 on basophils and mast cells in hu-HSC NOG IL-3/GM–Tg mice. BM mononuclear cells were collected from two hu-HSC NOG IL-3/GM–Tg mice 18 wk after HSC transplantation and stimulated with ionomycin. Human PBMCs were used as a positive control. The cells were stained with each Ab, and the levels of hCD63 in hCD45$^+$hCD203$^+$hFcεR$^+$ cells, with or without stimulation, are presented as graphs. Representative data are shown. $^*p < 0.05$, $^{**}p < 0.005$, $^{***}p < 0.0005$, $^{****}p < 0.00005$.

Tissue-resident human mast cells were identified by immunohistochemistry using anti-hMCC Abs (Fig. 5A). MCC$^+$ cells were abundant in the spleen in hu-HSC NOG IL-3/GM–Tg mice, whereas only a few MCC$^+$ cells were detected in non-Tg mice. Significant numbers of MCC$^+$ cells were also identified in the lungs and stomach of hu-HSC NOG IL-3/GM–Tg mice but not non-Tg mice. Generally, human mast cells are classified on the basis of their protease contents (38). Mast cells containing tryptase and chymase (MCTC) localize primarily in the skin and any other tissues and resemble the connective tissue–type mast cells in the rodent. In contrast, mast cells containing tryptase (MCTs) but not chymase are dominant in mucosal tissues, including the lung and gastric mucosa, similar to mucosal-type mast cells in rodents. To clarify the subtypes of human mast cells, we stained sections from the spleen, lung, stomach, and skin from humanized Tg or non-Tg mice with anti-chymase and anti-tryptase mAbs. We detected abundant MCTCs with tryptase and chymase, whereas few MCTs solely expressed tryptase (Fig. 5B).

Taken together, these results suggested that a large number of IgER-expressing human basophils and mast cells developed in IL-3/GM–Tg mice. These human mast cells resemble MCTCs and are distributed in various tissues, including mucosal tissues.

PCA responses in hu-HSC NOG IL-3/GM–Tg mice

Mast cells mediate allergic responses by releasing chemical substances, such as histamine or leukotrienes. A series of intracellular

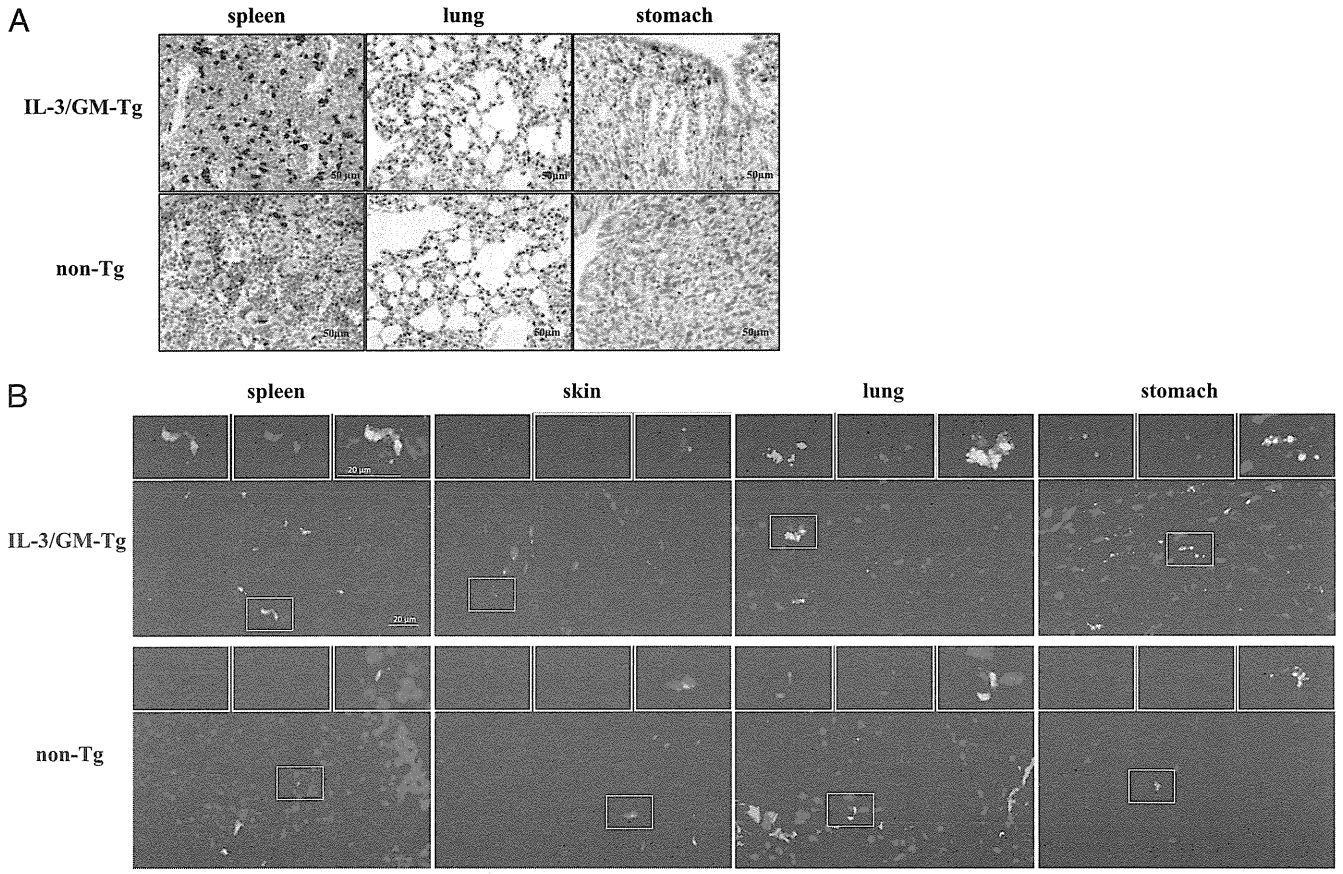

FIGURE 5. Histology of human mast cells in hu-HSC NOG IL-3/GM–Tg mice. (**A**) Detection of human mast cells by immunohistochemistry. Sections of various tissues from hu-HSC NOG IL-3/GM–Tg or non-Tg mice were stained with an anti-human MCC Ab. Each brown dot represents an individual human MCC-expressing mast cell. Representative images from five mice are shown. (**B**) Multicolor immunofluorescence analysis of human mast cells. Frozen sections of each tissue from Tg or non-Tg mice were stained with anti-human mast cell tryptase (green) and MCC (red) Abs. For double-labeled cells, the separate images were pseudo-colored, one as green and the other as red, and then merged to create the yellow color. Images shown are representative of one of three mice.

processes leading to degranulation of mast cells was triggered by cross-linking of IgE-bound FcεRI by specific Ags. The presence of a large number of human mast cells and basophils in hu-HSC NOG IL-3/GM–Tg mice prompted us to examine whether those cells could mediate Ag-specific IgE–dependent PCA reactions in vivo. Animals were sensitized with NP-specific IgE and challenged with NP-conjugated BSA 1 d later. As demonstrated in Fig. 6A, hu-HSC NOG IL-3/GM–Tg mice showed strong local inflammatory responses manifested by the extravasation of Evans blue dye, but much weaker in non-Tg mice. This was an Ag-specific reaction because the extravasation of the dye was detected only in the dorsal skin, and not on the ventral side, where control hIgE was administered. Furthermore, our examination showed that the PCA response was mediated by human cells, because nonhumanized NOG mice showed no extravasation of Evans blue dye, which eliminated the possibility that murine mast cells were activated by hIgE and hAg complexes. MCC staining confirmed the localization of a large number of human mast cells in both the dorsal and ventral skin of hu-HSC NOG IL-3/GM–Tg mice, with fewer human mast cells in non-Tg mice (Fig. 6B). Moreover, immunohistochemistry of the serial sections revealed that most of the FcεRI$^+$ cells in the dorsal skin of hu-HSC NOG IL-3/GM–Tg and non-Tg mice were positive for MCC (Fig. 6C), supporting that the PCA reaction was mediated by FcεRI-expressing human mast cells. Recently, Schafer et al. (39) demonstrated that the anaphylatoxins C3a and C5a enhance the IgE-mediated PCA reaction, including mast cell degranulation and inflammation, in mice. Indeed, we detected the expression of both hC3aR and hC5aR on mast cells in hu-HSC NOG IL-3/GM–Tg mice (Supplemental Fig. 2A). Then, to examine the role of the anaphylatoxins in our system, either C3aR or C5aR antagonist was administered to hu-HSC NOG IL-3/GM–Tg mice to inhibit binding of these anaphylatoxins on human mast cells during our NP-induced PCA responses. The PCA responses were strongly inhibited by the C3aR antagonist but not by the C5aR antagonist (Supplemental Fig. 2B, 2C). The modest effect of the C5aR antagonist may be attributed to the lack of murine C5 in NOD strains (40). These results suggest that the C3a anaphylatoxin plays an important role in the induction of PCA in hu-HSC NOG IL-3/GM–Tg mice.

We next examined whether the PCA reaction could be caused by patient-derived materials. We used the serum containing Japanese cedar pollen–specific hIgE obtained from pollinosis patients. After sensitization with the serum and subsequent injection with cedar pollen extract, strong extravasation of Evans blue dye into skin was detected in hu-HSC NOG IL-3/GM–Tg mice (Fig. 6D, 6E). Non-Tg mice showed a weak PCA reaction, probably due to the presence of only a few FcεRI$^+$ cells (Fig. 6B), which may react with hIgE (Fig. 6D, 6E).

Collectively, these results suggested that human mast cells differentiated in hu-HSC NOG IL-3/GM–Tg mice have sufficient capacity to mediate allergic inflammatory responses in vivo and that the effector phase of allergic responses manifested by histamine release can be fully recapitulated in our hu-HSC NOG IL-3/GM–Tg mice.

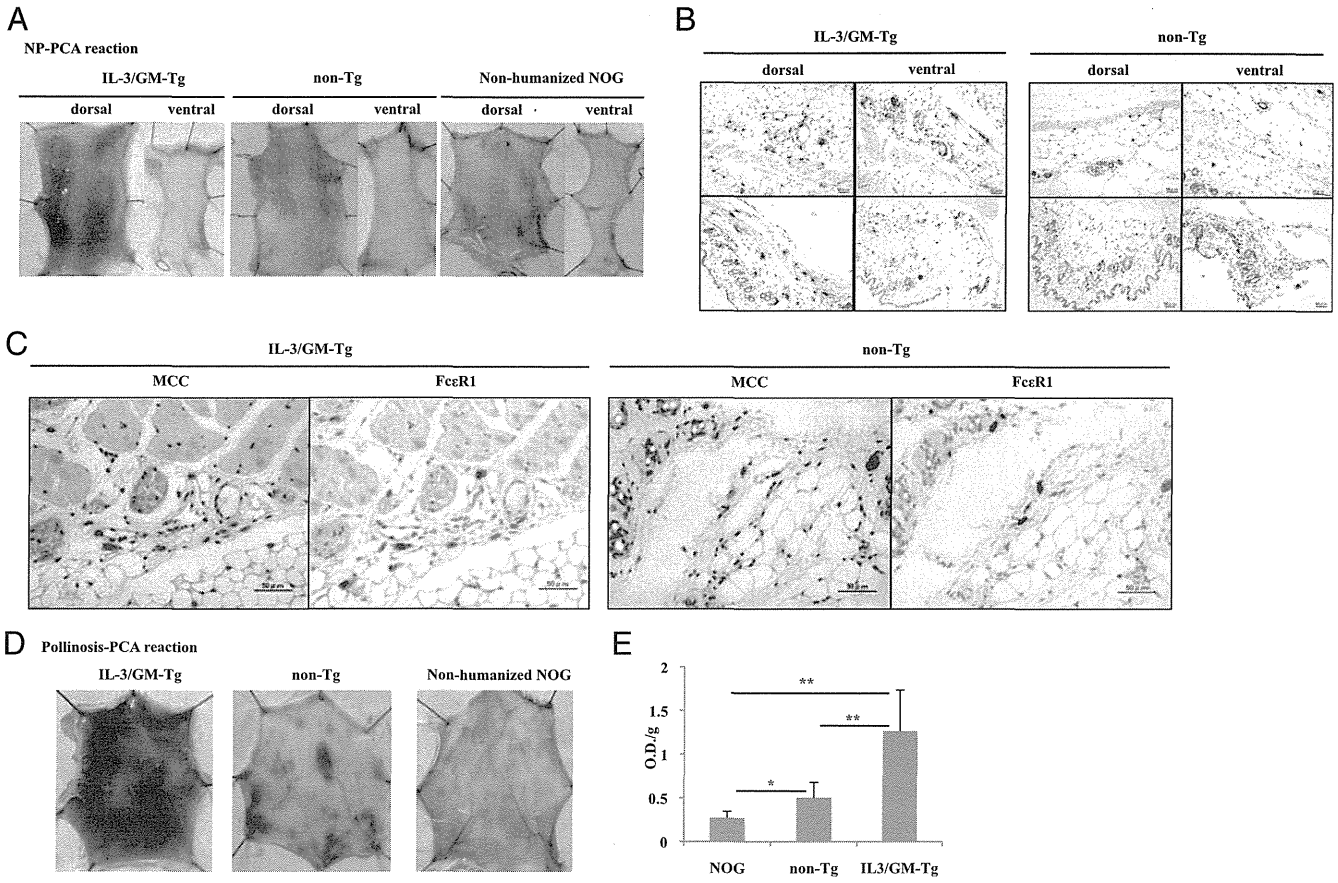

FIGURE 6. PCA reaction in hu-HSC NOG IL-3/GM–Tg mice. PCA was induced as described in *Materials and Methods*. (**A**) Extravasation of Evans blue dye in hu-HSC NOG IL-3/GM–Tg mice. Skin from dorsal (*left panels*) or ventral (*right panels*) sides was isolated from the indicated mice 30 min after systemic administration of NP and Evans blue dye. Representative images from two independent experiments using three mice are shown. (**B**) Localization of human mast cells in skin. After PCA sensitization, sections of dorsal and ventral skin from hu-HSC NOG IL-3/GM–Tg and non-Tg mice were stained with anti-human MCC Abs. Images of two fields from the indicated skin are shown. Each brown dot represents an individual human MCC-expressing mast cell. (**C**) Immunohistochemistry of the serial sections from skin. Skin samples from (B) were serially sectioned and stained with anti-human MCC and FcεRI Abs. (**D**) Extravasation of Evans blue dye in the skin of hu-HSC NOG IL-3/GM–Tg mice sensitized with the serum from Japanese cedar pollinosis patients. Dorsal skins were isolated from the hu-HSC NOG IL-3/GM–Tg (n = 6), non-Tg (n = 6), and nonhumanized NOG (n = 4) mice 30 min after systemic administration of a Japanese cedar pollen extract and Evans blue dye. Representative images of the dorsal skins are shown. (**E**) Quantification of Evans blue dye. The Evans blue dye in the skin was extracted with formamide, and the absorbance at 620 nm was measured using a spectrometer. $*p < 0.05$, $**p < 0.005$.

Discussion

In the current study, we demonstrated that a novel IL-3/GM–Tg NOG mouse substrain has a strong ability to promote the development of a variety of human myeloid cells from HSCs. Strikingly, developed human mast cells mediated allergic responses, as shown in PCA tests. To our knowledge, this is the first model to demonstrate that human cells generated in mice can mediate human allergic reactions in a reliable and repeatable manner.

Two immunodeficient mouse strains carrying the human *IL-3* and *GM-CSF* genes have been generated: IL-3/GM-CSF/SCF–Tg (SGM3-Tg) mice (30) and IL-3/GM-CSF-KI mice (41). It is noteworthy that there were considerable differences in phenotypes between our study and these previous studies. For example, in contrast to the high engraftment of hHSCs in our IL-3/GM–Tg mice, engraftment was reduced in SGM3-Tg mice compared with control mice, and there was no significant improvement in HSC engraftment in IL-3/GM–CSF–KI mice. In addition, there were no major differences in the frequency or number of macrophages, granulocytes, or T cells between IL-3/GM–CSF–KI mice and control mice. Those phenotypes were completely different from our IL-3/GM–Tg mice, which have the highest potential of these three strains from the point of view of HSC maintenance and myelopoiesis. These inconsistencies may be attributed, in part, to differences in the levels and distributions of cytokines. The amount of IL-3 was 4–6-fold higher in SGM3-Tg mice than in our IL-3/GM–Tg mice. Because high levels of IL-3 interfere with HSC proliferation, despite its pivotal role in the expansion of HSCs in in vitro culture systems (42), this increase in IL-3 in SGM3-Tg mice may explain the reduction in HSCs in SGM3-Tg mice. In IL-3/GM–CSF–KI mice, the expression patterns of hIL-3 and hGM-CSF were similar to those of endogenous mIL-3 and mGM-CSF. Accordingly, because of the high expression of GM-CSF, major effects were most evident in the lungs, where many human alveolar macrophages resided after HSC transplantation. Hence, the tissue-specific expression of IL-3 or GM-CSF in KI mice was sufficient for tissue-specific development and migration of human cells but not for systemically reconstituting entire human myeloid cells.

Intriguingly, the improved development of myeloid cells in our IL-3/GM–Tg mice was rather similar to that in the TPO-KI mice established by Rongvaux et al. (31), which also showed high engraftment of HSCs, enhanced myeloid cell development, and granulocyte differentiation. Although detailed analyses of granulocyte subpopulations have not been reported in TPO-KI mice,

Giemsa staining indicated the differentiation of neutrophil-like cells with highly lobulated nuclei, which were rarely detected in our IL-3/GM–Tg strain. Differences in cytokines (i.e., TPO versus IL-3/GM–CSF) influenced the lineage decisions of human myeloid cells, explaining the different results observed in these two strains.

The most striking characteristic of our NOG IL-3/GM–Tg strain was that a large number of fully functional human basophils and mast cells were able to develop from HSCs. The numbers of these cell populations in conventional humanized mice are too small in which to analyze the functional maturity and characteristics of these populations, especially in in vivo situations, although two reports demonstrated the presence of these cells in conventional NOG mice (43, 44). The initial study of human mast cells in humanized mice was reported by Kambe et al. (43). They showed that a few MCTs were present in the lung and stomach of conventional humanized NOG mice and that both types of human mast cells were differentiated in these animals. This result is inconsistent with our findings, and there might be several reasons for the discrepancy. Kambe et al. (43) identified these mast cell phenotypes by an immunoenzyme technique using anti-chymase (clone: B7) and anti-tryptase (clone: G3) mAbs, whereas we used directly labeled mAbs for our double-staining results. These different techniques and mAb clones could explain this inconsistency. Also, MCTs require IL-4 to suppress chymase expression (45). The production of IL-4 from human T cells in humanized mice was markedly lower than that in human PB, and there were large variances in the amounts of IL-4 in humanized mice (46). Varying levels of IL-4 may be responsible for the poor development of MCTs in our mouse colony. Therefore, administration of hIL-4 to humanized mice may support human mast cell development.

Recently, Takagi et al. (32) demonstrated that the development of human mast cells was significantly improved in their new hSCF-Tg NSG strain compared with normal NSG mice. However, the expression of hFcεRI on mast cells was not evaluated, and the ability of their strain to mediate human allergic responses in vivo was not addressed. Although IL-3/GM–Tg mice have no source of hSCF, the human mast cells developed in our IL-3/GM–Tg mice may be stimulated by mSCF, which is known to cross-react with human c-kit on mast cells (24). It will be interesting to compare the development of human mast cells between IL-3/GM–Tg and SCF-Tg mice, because this comparison may be useful in future investigations of human mast cells.

Previously, hIgE-mediated allergic responses were studied using hPBMC-engrafted mice (47–49). Weigmann et al. (49) demonstrated that colon inflammation was induced by rectal or oral challenge of allergens in NSG mice transplanted with allergic patient–derived hPBMCs. In these models, it is thought that patient-derived B cells produced an allergen-specific IgE Ab in mice, which, in turn, triggered allergic inflammation upon administration of the specific allergen. Although some aspects of allergic symptoms were mimicked in these models, suggesting that they may serve as an attractive model for human allergies, there are several caveats to the current study. For example, the release of histamine and any granules would become insufficient because of the small number of human basophils or mast cells in hPBMC grafts. In addition, xenogenic GVHD occurred easily in NOD-*scid*-IL2rγ^{null} mice when they were transplanted with hPBMCs (15). Xenogenic GVHD symptoms may sometimes be confused with allergic inflammation, and careful examinations are necessary. From these points, we conclude that our IL-3/GM–Tg mouse system is superior to PBMC-induced models because of the stable presence of many human mast cells and basophils in mouse environments; moreover, these cells did not develop GVHD, enabling long-term experimentation.

In summary, we generated a novel mouse strain, IL-3/GM–CSF–Tg NOG, which is one of the most suitable strains for inducing human hematopoiesis, including the production of granulocytes and mast cells, from HSCs. In addition, it is of note that the effector phase of the human allergic response was induced by in vivo–developed human mast cells. This new mouse strain will be an indispensable platform for analyzing human allergies in vivo. Furthermore, by combining this strain with other Tg strains expressing HLA, IL-4, or IL-21, the complete recapitulation of human allergies will be possible in humanized mice. These models will enable the analysis of cellular and molecular mechanisms responsible for allergies and may become useful tools for developing antiallergy drugs in the near future.

Acknowledgments

We thank Kazuho Wakui (WDB Co., Ltd., Tokyo, Japan) and Masashi Sasaki (JAC, Inc., Tokyo, Japan) for technical assistance, and Yu-you Ka (CIEA) and Yasuhiko Ando, Takuma Mizusawa, and Kayo Tomiyama (JAC, Inc.) for maintaining the animals.

Disclosures

The authors have no financial conflicts of interest.

References

1. Kotani, M., M. Matsumoto, A. Fujita, S. Higa, W. Wang, M. Suemura, T. Kishimoto, and T. Tanaka. 2000. Persimmon leaf extract and astragalin inhibit development of dermatitis and IgE elevation in NC/Nga mice. *J. Allergy Clin. Immunol.* 106: 159–166.
2. Iwata, A., K. Nishio, R. K. Winn, E. Y. Chi, W. R. Henderson, Jr., and J. M. Harlan. 2003. A broad-spectrum caspase inhibitor attenuates allergic airway inflammation in murine asthma model. *J. Immunol.* 170: 3386–3391.
3. Tsunematsu, M., T. Yamaji, D. Kozutsumi, R. Murakami, S. Kimura, and K. Kino. 2007. Establishment of an allergic rhinitis model in mice for the evaluation of nasal symptoms. *Life Sci.* 80: 1388–1394.
4. Roy, K., H. Q. Mao, S. K. Huang, and K. W. Leong. 1999. Oral gene delivery with chitosan–DNA nanoparticles generates immunologic protection in a murine model of peanut allergy. *Nat. Med.* 5: 387–391.
5. Li, X. M., G. Kleiner, C. K. Huang, S. Y. Lee, B. Schofield, N. A. Soter, and H. A. Sampson. 2001. Murine model of atopic dermatitis associated with food hypersensitivity. *J. Allergy Clin. Immunol.* 107: 693–702.
6. Bankert, R. B., S. V. Balu-Iyer, K. Odunsi, L. D. Shultz, R. J. Kelleher, Jr., J. L. Barnas, M. Simpson-Abelson, R. Parsons, and S. J. Yokota. 2011. Humanized mouse model of ovarian cancer recapitulates patient solid tumor progression, ascites formation, and metastasis. *PLoS ONE* 6: e24420.
7. Machida, K., H. Suemizu, K. Kawai, T. Ishikawa, R. Sawada, Y. Ohnishi, and T. Tsuchiya. 2009. Higher susceptibility of NOG mice to xenotransplanted tumors. *J. Toxicol. Sci.* 34: 123–127.
8. Suemizu, H., M. Monnai, Y. Ohnishi, M. Ito, N. Tamaoki, and M. Nakamura. 2007. Identification of a key molecular regulator of liver metastasis in human pancreatic carcinoma using a novel quantitative model of metastasis in NOD/SCID/gammacnull (NOG) mice. *Int. J. Oncol.* 31: 741–751.
9. Miyakawa, Y., Y. Ohnishi, M. Tomisawa, M. Monnai, K. Kohmura, Y. Ueyama, M. Ito, Y. Ikeda, M. Kizaki, and M. Nakamura. 2004. Establishment of a new model of human multiple myeloma using NOD/SCID/gammac(null) (NOG) mice. *Biochem. Biophys. Res. Commun.* 313: 258–262.
10. Libby, S. J., M. A. Brehm, D. L. Greiner, L. D. Shultz, M. McClelland, K. D. Smith, B. T. Cookson, J. E. Karlinsey, T. L. Kinkel, S. Porwollik, et al. 2010. Humanized nonobese diabetic-scid IL2rgammanull mice are susceptible to lethal *Salmonella typhi* infection. *Proc. Natl. Acad. Sci. USA* 107: 15589–15594.
11. Sato, K., N. Misawa, C. Nie, Y. Satou, D. Iwakiri, M. Matsuoka, R. Takahashi, K. Kuzushima, M. Ito, K. Takada, and Y. Koyanagi. 2011. A novel animal model of Epstein-Barr virus-associated hemophagocytic lymphohistiocytosis in humanized mice. *Blood* 117: 5663–5673.
12. Yajima, M., K. Imadome, A. Nakagawa, S. Watanabe, K. Terashima, H. Nakamura, M. Ito, N. Shimizu, M. Honda, N. Yamamoto, and S. Fujiwara. 2008. A new humanized mouse model of Epstein-Barr virus infection that reproduces persistent infection, lymphoproliferative disorder, and cell-mediated and humoral immune responses. *J. Infect. Dis.* 198: 673–682.
13. Sato, K., T. Izumi, N. Misawa, T. Kobayashi, Y. Yamashita, M. Ohmichi, M. Ito, A. Takaori-Kondo, and Y. Koyanagi. 2010. Remarkable lethal G-to-A mutations in vif-proficient HIV-1 provirus by individual APOBEC3 proteins in humanized mice. *J. Virol.* 84: 9546–9556.
14. Watanabe, S., K. Terashima, S. Ohta, S. Horibata, M. Yajima, Y. Shiozawa, M. Z. Dewan, Z. Yu, M. Ito, T. Morio, et al. 2007. Hematopoietic stem cell-engrafted NOD/SCID/IL2Rgamma null mice develop human lymphoid systems and induce long-lasting HIV-1 infection with specific humoral immune responses. *Blood* 109: 212–218.

15. Ito, R., I. Katano, K. Kawai, H. Hirata, T. Ogura, T. Kamisako, T. Eto, and M. Ito. 2009. Highly sensitive model for xenogenic GVHD using severe immunodeficient NOG mice. *Transplantation* 87: 1654–1658.
16. van Rijn, R. S., E. R. Simonetti, A. Hagenbeek, M. C. Hogenes, R. A. de Weger, M. R. Canninga-van Dijk, K. Weijer, H. Spits, G. Storm, L. van Bloois, et al. 2003. A new xenograft model for graft-versus-host disease by intravenous transfer of human peripheral blood mononuclear cells in RAG2$^{-/-}$ gammac$^{-/-}$ double-mutant mice. *Blood* 102: 2522–2531.
17. Ito, M., H. Hiramatsu, K. Kobayashi, K. Suzue, M. Kawahata, K. Hioki, Y. Ueyama, Y. Koyanagi, K. Sugamura, K. Tsuji, et al. 2002. NOD/SCID/gamma (c)(null) mouse: an excellent recipient mouse model for engraftment of human cells. *Blood* 100: 3175–3182.
18. Hiramatsu, H., R. Nishikomori, T. Heike, M. Ito, K. Kobayashi, K. Katamura, and T. Nakahata. 2003. Complete reconstitution of human lymphocytes from cord blood CD34+ cells using the NOD/SCID/gammacnull mice model. *Blood* 102: 873–880.
19. Yahata, T., K. Ando, Y. Nakamura, Y. Ueyama, K. Shimamura, N. Tamaoki, S. Kato, and T. Hotta. 2002. Functional human T lymphocyte development from cord blood CD34+ cells in nonobese diabetic/Shi-scid, IL-2 receptor gamma null mice. *J. Immunol.* 169: 204–209.
20. Shultz, L. D., B. L. Lyons, L. M. Burzenski, B. Gott, X. Chen, S. Chaleff, M. Kotb, S. D. Gillies, M. King, J. Mangada, et al. 2005. Human lymphoid and myeloid cell development in NOD/LtSz-scid IL2R gamma null mice engrafted with mobilized human hemopoietic stem cells. *J. Immunol.* 174: 6477–6489.
21. Traggiai, E., L. Chicha, L. Mazzucchelli, L. Bronz, J. C. Piffaretti, A. Lanzavecchia, and M. G. Manz. 2004. Development of a human adaptive immune system in cord blood cell-transplanted mice. *Science* 304: 104–107.
22. Goldman, J. P., M. P. Blundell, L. Lopes, C. Kinnon, J. P. Di Santo, and A. J. Thrasher. 1998. Enhanced human cell engraftment in mice deficient in RAG2 and the common cytokine receptor gamma chain. *Br. J. Haematol.* 103: 335–342.
23. Ito, M., K. Kobayashi, and T. Nakahata. 2008. NOD/Shi-scid IL2rgamma(null) (NOG) mice more appropriate for humanized mouse models. *Curr. Top. Microbiol. Immunol.* 324: 53–76.
24. Manz, M. G. 2007. Human-hemato-lymphoid-system mice: opportunities and challenges. *Immunity* 26: 537–541.
25. Egeland, T., R. Steen, H. Quarsten, G. Gaudernack, Y. C. Yang, and E. Thorsby. 1991. Myeloid differentiation of purified CD34+ cells after stimulation with recombinant human granulocyte-monocyte colony-stimulating factor (CSF), granulocyte-CSF, monocyte-CSF, and interleukin-3. *Blood* 78: 3192–3199.
26. Brugger, W., W. Möcklin, S. Heimfeld, R. J. Berenson, R. Mertelsmann, and L. Kanz. 1993. Ex vivo expansion of enriched peripheral blood CD34+ progenitor cells by stem cell factor, interleukin-1 beta (IL-1 beta), IL-6, IL-3, interferon-gamma, and erythropoietin. *Blood* 81: 2579–2584.
27. Petzer, A. L., P. W. Zandstra, J. M. Piret, and C. J. Eaves. 1996. Differential cytokine effects on primitive (CD34+CD38−) human hematopoietic cells: novel responses to Flt3-ligand and thrombopoietin. *J. Exp. Med.* 183: 2551–2558.
28. Ohmizono, Y., H. Sakabe, T. Kimura, S. Tanimukai, T. Matsumura, H. Miyazaki, S. D. Lyman, and Y. Sonoda. 1997. Thrombopoietin augments ex vivo expansion of human cord blood-derived hematopoietic progenitors in combination with stem cell factor and flt3 ligand. *Leukemia* 11: 524–530.
29. Piacibello, W., L. Fubini, F. Sanavio, M. F. Brizzi, A. Severino, L. Garetto, A. Stacchini, L. Pegoraro, and M. Aglietta. 1995. Effects of human FLT3 ligand on myeloid leukemia cell growth: heterogeneity in response and synergy with other hematopoietic growth factors. *Blood* 86: 4105–4114.
30. Billerbeck, E., W. T. Barry, K. Mu, M. Dorner, C. M. Rice, and A. Ploss. 2011. Development of human CD4+FoxP3+ regulatory T cells in human stem cell factor-, granulocyte-macrophage colony-stimulating factor-, and interleukin-3-expressing NOD-SCID IL2Rγ(null) humanized mice. *Blood* 117: 3076–3086.
31. Rongvaux, A., T. Willinger, H. Takizawa, C. Rathinam, W. Auerbach, A. J. Murphy, D. M. Valenzuela, G. D. Yancopoulos, E. E. Eynon, S. Stevens, et al. 2011. Human thrombopoietin knockin mice efficiently support human hematopoiesis in vivo. *Proc. Natl. Acad. Sci. USA* 108: 2378–2383.
32. Takagi, S., Y. Saito, A. Hijikata, S. Tanaka, T. Watanabe, T. Hasegawa, S. Mochizuki, J. Kunisawa, H. Kiyono, H. Koseki, et al. 2012. Membrane-bound human SCF/KL promotes in vivo human hematopoietic engraftment and myeloid differentiation. *Blood* 119: 2768–2777.
33. Fukuchi, Y., Y. Miyakawa, M. Kizaki, A. Umezawa, K. Shimamura, K. Kobayashi, T. Kuramochi, J. Hata, Y. Ikeda, N. Tamaoki, et al. 1999. Human acute myeloblastic leukemia-ascites model using the human GM-CSF- and IL-3-releasing transgenic SCID mice. *Ann. Hematol.* 78: 223–231.
34. Pawankar, R., M. Okuda, H. Yssel, K. Okumura, and C. Ra. 1997. Nasal mast cells in perennial allergic rhinitics exhibit increased expression of the Fc epsilonRI, CD40L, IL-4, and IL-13, and can induce IgE synthesis in B cells. *J. Clin. Invest.* 99: 1492–1499.
35. Yamaguchi, M., K. Sayama, K. Yano, C. S. Lantz, N. Noben-Trauth, C. Ra, J. J. Costa, and S. J. Galli. 1999. IgE enhances Fc epsilon receptor I expression and IgE-dependent release of histamine and lipid mediators from human umbilical cord blood-derived mast cells: synergistic effect of IL-4 and IgE on human mast cell Fc epsilon receptor I expression and mediator release. *J. Immunol.* 162: 5455–5465.
36. Suemizu, H., C. Yagihashi, T. Mizushima, T. Ogura, T. Etoh, K. Kawai, and M. Ito. 2008. Establishing EGFP congenic mice in a NOD/Shi-scid IL2Rg(null) (NOG) genetic background using a marker-assisted selection protocol (MASP). *Exp. Anim.* 57: 471–477.
37. Knol, E. F., F. P. Mul, H. Jansen, J. Calafat, and D. Roos. 1991. Monitoring human basophil activation via CD63 monoclonal antibody 435. *J. Allergy Clin. Immunol.* 88: 328–338.
38. Irani, A. A., N. M. Schechter, S. S. Craig, G. DeBlois, and L. B. Schwartz. 1986. Two types of human mast cells that have distinct neutral protease compositions. *Proc. Natl. Acad. Sci. USA* 83: 4464–4468.
39. Schafer, B., A. M. Piliponsky, T. Oka, C. H. Song, N. P. Gerard, C. Gerard, M. Tsai, J. Kalesnikoff, and S. J. Galli. 2013. Mast cell anaphylatoxin receptor expression can enhance IgE-dependent skin inflammation in mice. *J. Allergy Clin. Immunol.* 131: 541–548.e1–9.
40. Lynch, D. M., and P. H. Kay. 1995. Studies on the polymorphism of the fifth component of complement in laboratory mice. *Exp. Clin. Immunogenet.* 12: 253–260.
41. Willinger, T., A. Rongvaux, H. Takizawa, G. D. Yancopoulos, D. M. Valenzuela, A. J. Murphy, W. Auerbach, E. E. Eynon, S. Stevens, M. G. Manz, and R. A. Flavell. 2011. Human IL-3/GM-CSF knock-in mice support human alveolar macrophage development and human immune responses in the lung. *Proc. Natl. Acad. Sci. USA* 108: 2390–2395.
42. Zandstra, P. W., E. Conneally, A. L. Petzer, J. M. Piret, and C. J. Eaves. 1997. Cytokine manipulation of primitive human hematopoietic cell self-renewal. *Proc. Natl. Acad. Sci. USA* 94: 4698–4703.
43. Kambe, N., H. Hiramatsu, M. Shimonaka, H. Fujino, R. Nishikomori, T. Heike, M. Ito, K. Kobayashi, Y. Ueyama, N. Matsuyoshi, et al. 2004. Development of both human connective tissue-type and mucosal-type mast cells in mice from hematopoietic stem cells with identical distribution pattern to human body. *Blood* 103: 860–867.
44. Tanaka, S., Y. Saito, J. Kunisawa, Y. Kurashima, T. Wake, N. Suzuki, L. D. Shultz, H. Kiyono, and F. Ishikawa. 2012. Development of mature and functional human myeloid subsets in hematopoietic stem cell-engrafted NOD/SCID/IL2rγKO mice. *J. Immunol.* 188: 6145–6155.
45. Lorentz, A., and S. C. Bischoff. 2001. Regulation of human intestinal mast cells by stem cell factor and IL-4. *Immunol. Rev.* 179: 57–60.
46. Saito, Y., Y. Kametani, K. Hozumi, N. Mochida, K. Ando, M. Ito, T. Nomura, Y. Tokuda, H. Makuuchi, T. Tajima, and S. Habu. 2002. The in vivo development of human T cells from CD34(+) cells in the murine thymic environment. *Int. Immunol.* 14: 1113–1124.
47. Duez, C., A. Tsicopoulos, A. Janin, I. Tillie-Leblond, G. Thyphronitis, P. Marquillies, Q. Hamid, B. Wallaert, A. B. Tonnel, and J. Pestel. 1996. An in vivo model of allergic inflammation: pulmonary human cell infiltrate in allergen-challenged allergic Hu-SCID mice. *Eur. J. Immunol.* 26: 1088–1093.
48. Herz, U., V. A. Botchkarev, R. Paus, and H. Renz. 2004. Increased airway responsiveness, allergy-type-I skin responses and systemic anaphylaxis in a humanized-severe combined immuno-deficiency mouse model. *Clin. Exp. Allergy* 34: 478–487.
49. Weigmann, B., N. Schughart, C. Wiebe, S. Sudowe, H. A. Lehr, H. Jonuleit, L. Vogel, C. Becker, M. F. Neurath, S. Grabbe, et al. 2012. Allergen-induced IgE-dependent gut inflammation in a human PBMC-engrafted murine model of allergy. *J. Allergy Clin. Immunol.* 129: 1126–1135.